

Distilling and Transferring Knowledge via cGAN-generated Samples for Image Classification and Regression

Xin Ding^a, Yongwei Wang^{b,*}, Zuheng Xu^a, Z. Jane Wang^b, William J. Welch^a

^aDepartment of Statistics, University of British Columbia, Vancouver, BC, V6T 1Z4, Canada

^bDepartment of Electrical and Computer Engineering, University of British Columbia, Vancouver, BC, V6T 1Z4, Canada

Abstract

Knowledge distillation (KD) has been actively studied for image classification tasks in deep learning, aiming to improve the performance of a student model based on the knowledge from a teacher model. However, applying KD in image regression with a scalar response variable is also important (e.g., age estimation) yet has been rarely studied. Besides, existing KD methods often require a practitioner to carefully select or adjust the teacher and student architectures, making these methods less flexible in practice. To address the above problems in a unified way, we propose a comprehensive KD framework based on *conditional generative adversarial networks* (cGANs), termed cGAN-KD. Fundamentally different from existing KD methods, cGAN-KD distills and transfers knowledge from a teacher model to a student model via specifically processed cGAN-generated samples. This novel mechanism makes cGAN-KD suitable for both classification and regression tasks, compatible with other KD methods, and insensitive to the teacher and student architectures. An error bound for a student model trained in the cGAN-KD framework is derived in this work, providing a theory for why cGAN-KD is effective as well as guiding the practical implementation of cGAN-KD. Extensive experiments on CIFAR-100 and ImageNet-100 (a subset of ImageNet with only 100 classes) datasets show that the cGAN-KD framework can leverage state-of-the-art KD methods to yield a new state of the art. Moreover, experiments on Steering Angle and UTKFace datasets demonstrate the effectiveness of cGAN-KD in image regression tasks. Notably, in classification, incorporating cGAN-KD into training improves the state-of-the-art SSKD by an average of 1.32% in test accuracy on ImageNet-100 across five different teacher-student pairs. In regression, cGAN-KD decreases the test mean absolute error of a WRN16×1 student model from 5.74 to 1.79 degrees (i.e., 68.82% drop) on Steering Angle.

Keywords: knowledge distillation, unified framework, conditional generative adversarial networks

1. Introduction

The high precision of a heavyweight learning model, often a deep, overparameterized neural network or an ensemble of multiple deep neural networks, usually comes with associated costs. First, the large model size (i.e., many learnable parameters) implies a high memory cost. Secondly, the complexity leads to a low inference speed, i.e., the number of images processed per second. Thus, limited computational resources to evaluate a trained model (e.g., deploying neural networks on mobile devices), require the deployment of a lightweight model that is memory-efficient and fast in inference. The *small model capacity* of a lightweight model would often lead to lower precision, however, motivating recent increased attention on leveraging an accurate heavyweight model to improve the performance of a lightweight model.

Knowledge distillation (KD), first proposed by Buciluă et al. (2006) and then developed by Hinton et al. (2015), is a popular method to improve the performance of a lightweight model by utilizing the knowledge

*Corresponding author.

Email addresses: dingx92ubc@126.com (Xin Ding), yongweiw@ece.ubc.ca (Yongwei Wang), zuheng.xu@stat.ubc.ca (Zuheng Xu), zjanew@ece.ubc.ca (Z. Jane Wang), will@stat.ubc.ca (William J. Welch)

distilled from an accurate, heavyweight model. The heavyweight and lightweight models in KD are often known respectively as a *teacher* model and a *student* model. After Hinton et al. (2015) introduced *baseline knowledge distillation* (BLKD), many KD methods have been proposed for the image classification task (Wang & Yoon, 2021; Gou et al., 2021). These methods can be categorized as logit-based KD (Hinton et al., 2015; Mirzadeh et al., 2020), feature-based KD (Romero et al., 2015; Zagoruyko & Komodakis, 2017; Kim et al., 2018; Ahn et al., 2019; Heo et al., 2019; Chen et al., 2021b,a; Wang et al., 2022; Chen et al., 2022), relation-based KD (Passalis & Tefas, 2018; Tung & Mori, 2019; Park et al., 2019), self-supervised KD (Tian et al., 2019; Xu et al., 2020), etc. To transfer knowledge, these KD methods often need to define new loss functions or design new auxiliary training tasks (e.g., the self-supervised learning task). Consequently, we often need to carefully choose teacher models or adjust the network architectures of the teacher and student models, making the implementation of these KD methods complicated.

Unlike the image classification task, the application of KD in image regression with a scalar response variable (e.g., the angle and age applications studied in Section 5) has rarely been studied. Zhao et al. (2020a) propose a KD method specially designed to estimate ages from human face images. However, this method does not apply to general image regression tasks with a scalar response because some techniques of the proposed framework are only applicable for age estimation. Saputra et al. (2019) propose a KD framework to transfer knowledge from a large pose estimation network to a small one. However, the response variable in pose estimation is multivariate which distinguishes from a scalar variable in isometric characteristics. Besides, the proposed KD method in Saputra et al. (2019) is only applicable to some specific network architectures. There is no practical KD method general enough for image regression tasks with a scalar response to our best knowledge. Moreover, all the above methods are designed specifically for either image classification or image regression; there exists no unified KD framework suitable for both tasks yet.

Generative adversarial networks (GANs) are state-of-the-art generative models for image synthesis (Goodfellow et al., 2014; Mirza & Osindero, 2014; Odena et al., 2017; Miyato et al., 2018; Zhang et al., 2019; Brock et al., 2019; Miyato & Koyama, 2018; Karras et al., 2019, 2020b; Ding et al., 2021a,b; Zhou et al., 2021; Li et al., 2021). Some modern GAN models such as BigGAN (Brock et al., 2019) and StyleGAN (Karras et al., 2019, 2020b) are able to generate high-resolution, even photo-realistic images. *Conditional generative adversarial networks* (cGANs) are a type of GANs that can generate images in terms of certain conditions. Most cGANs are designed for categorical conditions such as class labels (Mirza & Osindero, 2014; Miyato & Koyama, 2018; Odena et al., 2017; Miyato et al., 2018; Zhang et al., 2019; Brock et al., 2019; Xu et al., 2021), and cGANs with class labels as conditions are also known as *class-conditional GANs*. Recently, Ding et al. (2021a,b) propose a new cGAN framework, termed *continuous conditional GANs* (CcGANs). CcGANs can generate images conditional on continuous, scalar variables (termed *regression labels*). In the scenario with limited training data, the performance of GANs often deteriorates. To alleviate this problem for unconditional GANs and class-conditional GANs, DiffAugment (Zhao et al., 2020b) proposes to conduct online transformation on images during the GAN training. Our experiments show that it also applies to CcGANs. Besides the advances in GAN theory, Frid-Adar et al. (2018), Sixt et al. (2018), Wu et al. (2018), Zhu et al. (2018), Mariani et al. (2018), and Ali-Gombe & Elyan (2019) use GAN-generated data for data augmentation in image classification tasks with insufficient training data. However, even state-of-the-art GANs may generate low-quality samples, which may negatively affect the classification task. Fortunately, some recently proposed subsampling methods (Ding et al., 2020, 2022) may be applied to eliminate these low-quality samples. Additionally, some works (Xu et al., 2018; Wang et al., 2018; Shen et al., 2019; Liu et al., 2020) propose to incorporate the adversarial loss into KD, but their performance is not state of the art.

Motivated by the limitations of existing KD methods and the recent advances of cGANs, we propose a general and flexible KD framework applicable for both image classification and regression (with a scalar response). Our contributions can be summarized as follows:

- In Section 3, we introduce the proposed cGAN-KD framework, which distills and transfers knowledge via cGAN-generated samples. Compared with other methods, cGAN-KD is a unified KD framework suitable for both classification and regression tasks (with a scalar response). It is also compatible with state-of-the-art KD methods, where cGAN-KD can be incorporated into these methods to reach a new state of the art. Moreover, cGAN-KD is insensitive to architectural differences between teacher and student networks.

- In Section 4, we derive the error bound of a student model trained in the cGAN-KD framework, which not only helps us understand how cGAN-KD takes effect but also guides the implementation of cGAN-KD in practice. Such an analysis is often omitted in knowledge distillation papers. The error bound suggests that we should generate as many processed fake samples as possible and choose a teacher model with high precision.
- In Section 5, we conduct extensive experiments on CIFAR-100 (Krizhevsky et al., 2009), ImageNet-100 (Cao et al., 2017), Steering Angle (Chen, 2018b,a), and UTKFace (Zhang et al., 2017) to demonstrate the effectiveness of the cGAN-KD framework over state-of-the-art KD methods in both classification and regression tasks. We carefully design an ablation study to investigate the influence of different (sub-)modules of cGAN-KD. Several sensitivity analyses are also conducted to research the effects of cGAN-KD’s hyper-parameters.

2. Related work

In this section, we first provide a comprehensive review of representative knowledge distillation methods proposed for image classification and regression tasks. We then briefly introduce conditional generative adversarial networks (cGANs) and the subsampling techniques for cGANs.

2.1. Knowledge distillation

Logits-based KD. Hinton et al. proposed an effective logits-based knowledge distillation method (aka BLKD) that transfers knowledge from the teacher model to the student model by matching the *logits* (i.e., the output of the last layer in a neural network) between these two models. BLKD does not need to change the teacher and student models’ architectures, and it has been widely applied in visual recognition applications, e.g., image classification and face recognition (Gou et al., 2021).

Denote by \mathbf{l} the logits of an image \mathbf{x} from a neural network, where $\mathbf{l} = [l_1, \dots, l_C]^\top$ is a C by 1 vector and C is the number of classes. With softmax function, we can calculate the probability that the image \mathbf{x} belonging to class c as follows:

$$p_c = \frac{\exp(l_c/T)}{\sum_{k=1}^C \exp(l_k/T)}, \quad (1)$$

where $c = 1, \dots, C$ and T is the temperature factor. The C by 1 vector $\mathbf{p} = [p_1, \dots, p_C]^\top$ is also known as the *soft label* of image \mathbf{x} . A higher T leads to a softer probability distribution over classes. On the contrary, the one-hot encoded class label is also known as the *hard label*. An example of hard labels and soft labels is shown in Fig. 1. Usually, the soft label is more informative than the hard label because it can reflect the similarity between classes and the confidence of prediction. The logits of the same image \mathbf{x} from the teacher model f_t and the student model f_s are denoted by \mathbf{l}^t and \mathbf{l}^s respectively. Then, the corresponding soft labels are denoted respectively by \mathbf{p}^t and \mathbf{p}^s . The student model f_s is trained to minimize the cross entropy between \mathbf{p}^t and \mathbf{p}^s as follows:

$$\mathcal{L}_{KD} = \sum_{c=1}^C \{-p_c^t \log p_c^s\}. \quad (2)$$

The student model is also trained to minimize the cross entropy between the one-hot encoded class label \mathbf{y} and the soft label \mathbf{p}^s as follows:

$$\mathcal{L}_s = \sum_{c=1}^C \{-y_c \log p_c^s\}. \quad (3)$$

Finally, the overall training loss of f_s is a linear combination of Eqs. (2) and (3), i.e.,

$$\mathcal{L}_{overall} = (1 - \lambda_{KD})\mathcal{L}_s + \lambda_{KD}\mathcal{L}_{KD}, \quad (4)$$

where $\lambda_{KD} \in [0, 1]$ is a hyperparameter controlling the trade-off between two losses. \mathcal{L}_s is the standard loss for classification and \mathcal{L}_{KD} encourages the knowledge transfer.

Despite the simplicity and general effectiveness of BLKD, Mirzadeh et al. (2020) recently show that BLKD may not perform well if there exists a big performance gap between a teacher model and a student



Fig. 1: Example of hard and soft labels of a dog image in a 3-class classification task.

model. To resolve this issue, the authors introduce a *teacher assistant* (TA) model, which often performs better than the student model but worse than the teacher model. BLKD is applied to the teacher-TA and TA-student pairs, respectively, where the knowledge is first transferred from the teacher model to the TA model and then from the TA model to the student model.

Feature-based KD. Instead of matching logits only, feature-based KD methods also encourage the student to mimic the teacher in terms of intermediate feature representations. FitNet (Romero et al., 2015) is the first work that proposes to utilize feature responses as knowledge hints. FitNet works by minimizing the feature map discrepancy in the middle feature level between a teacher network and a student network that is deeper and thinner than its teacher. Based on feature maps, the *attention transfer* (AT) knowledge distillation (Zagoruyko & Komodakis, 2017) computes the activation-based and gradient-based attention maps, and transfers such attention knowledge to better guide the student model. Instead of directly utilizing or transforming feature maps, Kim et al. (2018) propose the *factorization transfer* (FT), which involves a paraphraser and a translator parameterized by convolutional modules. FT re-interprets and aligns the teacher’s and student’s feature responses. *Variational information distillation* (VID) (Ahn et al., 2019) and *activation boundary* (AB) (Heo et al., 2019) are another two novel feature-based KD methods that respectively maximize the mutual information and match the activation boundary between the teacher and student networks. To resolve the manual selection problem of intermediate layers between the teacher and student networks, Chen et al. (2021a) and Wang et al. (2022) propose semantic calibration for cross-layer knowledge distillation (SemCKD). SemCKD develops an attention mechanism to perform automatic layer association assignments. Recently, ReviewKD (Chen et al., 2021b) develops a knowledge review framework which explores the importance of low-level features in a teacher model. ReviewKD distills and transfers knowledge from multi-layers of a teacher model to supervise a student model. *Simple knowledge distillation* (SimKD) (Chen et al., 2022) is another very recent feature-based KD method. SimKD reuses the discriminative classifier from the pre-trained teacher for student inference and minimizes a ℓ_2 loss defined in the preceding layer of the final classifier. While feature-based KD methods show much potential in knowledge transfer, the architectural differences between the student and teacher networks may hinder their distillation effectiveness in practice.

Relation-based KD. The relation-based KD models the relational knowledge based on responses of different training samples. Passalis & Tefas (2018) propose a *probabilistic knowledge transfer* (PKT) method. PKT establishes a probabilistic version of the relational matrix using pairwise neighboring samples, then aligns the student with the teacher by minimizing the Kullback-Leibler of conditional probability distribution (i.e., each row of a relational matrix). Based on an observation that semantically similar samples produce similar activation, Tung & Mori (2019) propose the *similarity preserving* (SP) knowledge distillation method. A similarity matrix is computed from a batch of training samples at the feature level, and then it is used as auxiliary information to guide the student’s training. Similar to SP, Park et al. (2019) propose the *relational knowledge distillation* (RKD). RKD models the interplay between training samples by proposing a two-tuple distance-wise relation and a three-tuple angular-wise relation based on network embeddings. By capturing the structural relations among samples, the relation-based KD can distill additional informative knowledge and transfer it from the teacher to the student model.

Self-supervision signal-guided KD. Besides distilling representational knowledge from a regularly trained classifier, some recent works investigate the feasibility of extracting and transferring knowledge from self-supervision signals (Chen et al., 2020). Tian et al. (2019) propose a *contrastive representation distillation* (CRD) method that formulates a contrastive objective for training the teacher and the student models. CRD pushes closer the representations of a teacher and a student for the same sample; while it pushes far away

those from different samples. Xu et al. (2020) propose *self-supervised knowledge distillation* (SSKD). SSKD introduces the self-supervised learning scheme into knowledge distillation. Firstly, a pre-trained teacher model is tuned on a self-supervision pretask to learn generic representations in an unsupervised manner. Then, SSKD encourages the student model to mimic the teacher model in terms of both classification outputs (like BLKD) and self-supervision predictions.

Other related methods. In addition to the state-of-the-art representative KD methods above, there are two other types of KD methods that have gained attention, i.e., GAN-related KD methods (Xu et al., 2018; Wang et al., 2018; Shen et al., 2019; Liu et al., 2020) and data-free KD methods (Lopes et al., 2017; Chen et al., 2019; Yin et al., 2020). However, there also exist major distinctions to our method though they seem related to our method. Our cGAN-KD is fundamentally different from the GAN-related KDs: (1) cGAN-KD utilizes cGAN-generated samples to distill and transfer knowledge, while GAN-related KDs only incorporate adversarial losses into conventional KD methods (e.g., Hinton et al. (2015)), and they cannot achieve the state-of-the-art performance. (2) Our KD framework applies to both classification and regression tasks, while KD methods in GAN-related KDs can only apply to classification tasks. Our method also has quite different mechanisms to data-free KDs: (1) cGAN-KD uses a cGAN to synthesize fake samples instead of an inverted convolutional neural network; (2) cGAN-KD has a subsampling module and a label adjustment module to push the distribution of fake image-label pairs close to the actual distribution, but data-free KDs do not have these crucial techniques; and (3) The student is trained on both real and fake samples in cGAN-KD while data-free KDs do not have access to real samples.

2.2. Conditional generative adversarial networks

cGANs (Mirza & Osindero, 2014) aim to estimate the distribution of images conditional on some auxiliary information. A cGAN model includes two neural networks, a generator $G(\mathbf{z}, y)$ and a discriminator $D(\mathbf{x}, y)$. The generator $G(\mathbf{z}, y)$ takes as input a random noise $\mathbf{z} \sim N(\mathbf{0}, \mathbf{I})$ and the condition y , and outputs a fake image \mathbf{x}^g which follows the fake conditional image distribution $p_g(\mathbf{x}|y)$. The discriminator $D(\mathbf{x}, y)$ takes as input an image \mathbf{x} and the condition y , and outputs the probability that the image \mathbf{x} comes from the true conditional image distribution $p_r(\mathbf{x}|y)$. A typical pipeline of cGAN is shown in Fig. 2. Mathematically, the cGAN model is trained to minimize the divergence between $p_r(\mathbf{x}|y)$ and $p_g(\mathbf{x}|y)$. The condition y is usually a categorical variable such as a class label. cGANs with class labels as conditions are also known as *class-conditional GANs* (Mirza & Osindero, 2014; Miyato & Koyama, 2018; Odena et al., 2017; Miyato et al., 2018; Zhang et al., 2019; Brock et al., 2019). Class-conditional GANs have been widely studied, and the state-of-the-art models such as BigGAN (Brock et al., 2019) are already able to generate photo-realistic images. However, GANs conditional on regressions labels (e.g., angles and ages) have been rarely studied because of two problems. First, very few (even zero) images exist for some regression labels, so the empirical cGAN losses may fail. Second, since regression labels are continuous and infinitely many, they cannot be embedded by one-hot encoding like class labels. Recently, Ding et al. (2021a,b) propose a new formulation of cGANs, termed *CcGANs*. The CcGAN framework consists of novel empirical cGAN losses and novel label input mechanisms. To solve the first problem, the discriminator is trained by either the *hard vicinal discriminator loss* (HVDL) or the *soft vicinal discriminator loss* (SVDL). A new empirical generator loss is also proposed to alleviate the first problem. To solve the second problem, Ding et al. (2021a,b) introduce a *naive label input* (NLI) mechanism and an *improved label input* (ILI) mechanism. Hence, Ding et al. (2021a,b) propose four CcGAN models employing different discriminator losses and label input mechanisms, i.e., HVDL+NLI, SVDL+NLI, HVDL+ILI, and SVDL+ILI. The effectiveness of CcGANs has been demonstrated on multiple regression-oriented datasets, e.g., Steering Angle (Ding et al., 2021a,b) and UTKFace (Zhang et al., 2017).

The performance of cGANs often deteriorates when training data are insufficient. *DiffAugment* (Zhao et al., 2020b) is one of some recent works (Zhao et al., 2020b; Karras et al., 2020a; Tran et al., 2021; Zhao et al., 2020c) that are designed to stabilize the cGAN training in this setting. Although DiffAugment is designed for unconditional (e.g., styleGAN (Karras et al., 2019, 2020b)) and class-conditional GANs (e.g., BigGAN), our experiment shows that it is also applicable to CcGANs.

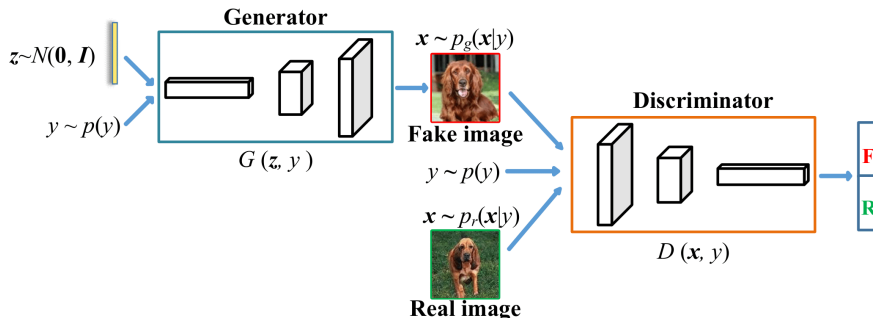


Fig. 2: **A typical pipeline of cGAN.** The conditioning variable y (e.g., y represents the class label or regression label) is assumed to follow a distribution $p(y)$, which can be easily estimated from the training data.

2.3. cDR-RS: Subsampling cGANs

Modern cGANs are demonstrated successful in many applications, but low-quality samples still appear frequently even with state-of-the-art network architectures (e.g., BigGAN) and training setups. To filter out low-quality samples, Ding et al. (2022) proposes a subsampling framework, termed *cDR-RS*, for class-conditional GANs and CcGANs. This framework consists of two components: a *conditional density ratio estimation* (cDRE) method termed *cDRE-F-cSP* and a *rejection sampling* (RS) scheme. cDRE-F-cSP aims to estimate the conditional density ratio function $r^*(\mathbf{x}|y) := p_r(\mathbf{x}|y)/p_g(\mathbf{x}|y)$. It trains a density ratio (DR) model (a neural network) to approximate $r^*(\mathbf{x}|y)$ based on N^r real images $\mathbf{x}_1^r, \mathbf{x}_2^r, \dots, \mathbf{x}_{N^r}^r \sim p_r(\mathbf{x}|y)$ and N^g fake images $\mathbf{x}_1^g, \mathbf{x}_2^g, \dots, \mathbf{x}_{N^g}^g \sim p_g(\mathbf{x}|y)$. Based on the estimated conditional density ratios, the rejection sampling scheme is utilized to sample from a trained cGAN. For class-conditional GANs, Ding et al. (2022) demonstrate that cDR-RS can substantially improve the *Fréchet inception distance* (FID) (Heusel et al., 2017) and Intra-FID (Miyato & Koyama, 2018) scores. For CcGANs, cDR-RS not only improves the Intra-FID score but also improves the image diversity and label consistency (i.e., the consistency of generated images with respect to the conditioning label) (Ding et al., 2021a; DeVries et al., 2019).

3. Proposed method

While many KD methods have been proposed for image classification, there is only one KD method for image regression (with a scalar response) (Zhao et al., 2020a). Unfortunately, it is specially designed for age estimation with specific network architectures and is not applicable as a general KD method for image regression with a scalar response. Moreover, there is no KD framework for both types of tasks.

This section proposes a unified KD framework, termed *cGAN-KD*, which is suitable for both image classification and regression (with a scalar response) tasks. The proposed framework can also fit into many state-of-the-art KD methods for image classification to improve their performances. In addition, we can blindly use the most precise heavyweight model as a teacher in cGAN-KD without worrying about the architectural difference between teacher and student.

To aid the reader, we summarize in Table 1 some essential notations with their definitions that appeared in this paper. These notations are also defined in detail near their first appearance.

3.1. Problem formulation

Before we introduce cGAN-KD, let us formulate the KD task mathematically as follows. Assume we have a set of N^r image-label pairs, i.e.,

$$D^r = \{(\mathbf{x}_i^r, y_i^r) \mid i = 1, \dots, N^r\},$$

which are randomly drawn from the actual image-label distribution with density function $p_r(\mathbf{x}, y)$. We also have a teacher model f_t and a student model f_s which are trained on D^r . f_t often has a smaller test error (i.e., higher precision) than f_s does, i.e.,

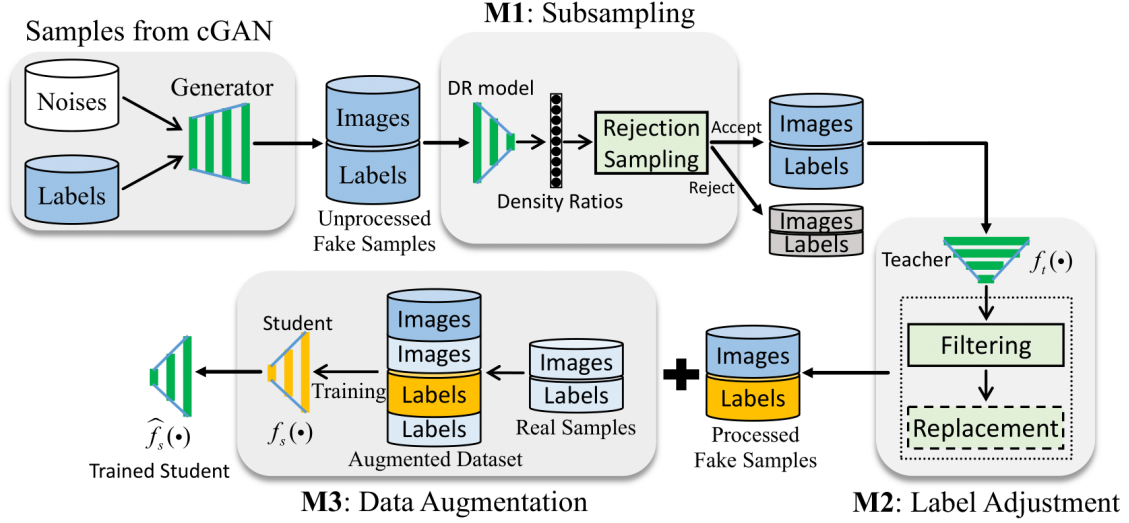


Fig. 3: **The workflow of the proposed cGAN-KD.** Three important modules are denoted respectively by **M1**, **M2**, and **M3**. **M2** has two sequential sub-modules, the *filtering* sub-module and the *replacement* sub-module. The replacement sub-module is enabled for regression only. **M1** aims to drop low-quality fake samples. **M2** distills knowledge from teacher and embeds it into fake samples. As a side effect, the filtering sub-module in **M2** can also help drop visually unrealistic images. Processed fake samples are then used to do data augmentation in **M3**, where the knowledge from the teacher is transferred to the student.

$$\mathbb{E}_{(\mathbf{x}, y) \sim p_r(\mathbf{x}, y)} \mathcal{L}(f_t(\mathbf{x}), y) \leq \mathbb{E}_{(\mathbf{x}, y) \sim p_r(\mathbf{x}, y)} \mathcal{L}(f_s(\mathbf{x}), y),$$

where \mathcal{L} is either the *cross entropy* (CE) loss (i.e., Eq. (2)) for classification or the *squared error* (SE) loss for regression. The objective of KD is to reduce the test error of f_s by using the knowledge learned by f_t .

3.2. The workflow of cGAN-KD

As a preliminary of cGAN-KD, we need to train a cGAN on D^r . For image classification, we suggest adopting state-of-the-art class-conditional GANs such as BigGAN (Brock et al., 2019). For image regression with a scalar response, we should use CcGANs (Ding et al., 2021a,b). In the scenario with very few training data, we propose to apply DiffAugment (Zhao et al., 2020b) to stabilize the cGAN training.

After the cGAN training, the proposed KD framework can be applied. In Fig. 3, we show the workflow of cGAN-KD, which includes three important modules denoted respectively by **M1** (*subsampling*), **M2** (*label adjustment*), and **M3** (*data augmentation*). Firstly, we can sample infinitely many unprocessed fake samples from the trained cGAN, i.e.,

$$D^g = \{(\mathbf{x}_i^g, y_i^g) \mid i = 1, \dots, +\infty\},$$

where (\mathbf{x}_i^g, y_i^g) is the i -th fake image-label pair. These fake samples are then subsampled by **M1** to drop low-quality ones and form a subset of D^g , i.e.,

$$D_s^g = \left\{ (\mathbf{x}_{(i)}^g, y_{(i)}^g) \mid (\mathbf{x}_{(i)}^g, y_{(i)}^g) \in D^g, i = 1, \dots, N^g \right\}.$$

The next module **M2** in the pipeline adjusts the labels of images in D_s^g by a pre-trained, precise teacher model f_t . **M2** has two sequential sub-modules, the filtering sub-module and the replacement sub-module. The output of **M2** is a set of processed samples, i.e.,

$$D_\rho^g = \begin{cases} \tilde{D}_\rho^g & \text{for classification,} \\ \hat{D}_\rho^g & \text{for regression.} \end{cases}$$

Table 1: Definitions of some essential notations in this paper.

Notation	Definition
\mathbf{x}	an image at $C \times H \times W$ resolution and it may have a subscript, a superscript, or a tilde, e.g., $\tilde{\mathbf{x}}_i^g$
y	a class/regression label and it may have a subscript or superscript, e.g., y_i^r
\hat{y}	a predicted class/regression label and it may have subscript or superscript, e.g., \hat{y}_i^r .
$p_r(\mathbf{x}, y)$	the density function of the joint distribution of real image-label pairs
$p_g(\mathbf{x}, y)$	the density function of the joint distribution of unprocessed fake image-label pairs
$p_g^s(\mathbf{x}, y)$	the density function of the joint distribution of fake image-label pairs after applying M1
$\tilde{p}_g^s(\mathbf{x}, y)$	the density function of the joint distribution of fake image-label pairs after applying filtering
$\hat{p}_g^s(\mathbf{x}, y)$	the density function of the joint distribution of fake image-label pairs after applying replacement
$p_g^p(\mathbf{x}, y)$	the density function of the joint distribution of fake image-label pairs after applying M2
D^r	a dataset of N^r real image-label pairs
D^g	a dataset of infinite unprocessed fake image-label pairs
D_s^g	a dataset of N^g fake image-label pairs after applying M1
\tilde{D}_ρ^g	a dataset of M^g fake image-label pairs after applying filtering
\hat{D}_ρ^g	a dataset of M^g fake image-label pairs after applying replacement
D_ρ^g	a dataset of M^g fake image-label pairs after applying M2 ; it equals either \tilde{D}_ρ^g or \hat{D}_ρ^g
D_{aug}	the augmented dataset in M3 , i.e., $D_{\text{aug}} := D^r \cup D_\rho^g$
α	the filtering threshold in M2 which is controlled by a hyper-parameter ρ or a class label c
ρ	a hyper-parameter in $[0, 1]$ to define the filtering threshold in M2 , representing the ρ -th quantile of some errors
$\mathcal{L}(\cdot, \cdot)$	a <i>cross entropy</i> (CE) loss for classification or a <i>squared error</i> (SE) loss for regression
f	a predictor for classification or regression
f^*	a theoretically optimal predictor
f_t	the pre-trained teacher model in cGAN-KD
f_s	the student model in cGAN-KD
\mathcal{F}_s	the hypothesis space of f_s , i.e., a set of functions that can be represented by f_s
$\widehat{\mathcal{R}}_{N^r+M^g}(\mathcal{F}_s)$	Empirical Rademacher complexity of \mathcal{F}_s in terms of N^r real samples and M^g fake samples.
$\mathcal{V}(f)$	$\mathcal{V}(f) := \mathbb{E}_{(\mathbf{x}, y) \sim p_r(\mathbf{x}, y)} [\mathcal{L}(f(\mathbf{x}), y)]$
$\widehat{\mathcal{V}}(f)$	$\widehat{\mathcal{V}}(f) := \frac{1}{N^r+M^g} \sum_{(\mathbf{x}_i, y_i) \in D_{\text{aug}}} \mathcal{L}(f(\mathbf{x}_i), y_i)$
f_s°	the theoretical minimizer, i.e., $f_s^\circ = \arg \min_{f_s \in \mathcal{F}_s} \mathcal{V}(f_s)$
\hat{f}_s	the empirical minimizer, i.e., $\hat{f}_s = \arg \min_{f_s \in \mathcal{F}_s} \widehat{\mathcal{V}}(f_s)$

\tilde{D}_ρ^g and \hat{D}_ρ^g are defined respectively as follows:

$$\tilde{D}_\rho^g = \begin{cases} \{(\tilde{\mathbf{x}}_i^g, \tilde{y}_i^g) \mid (\tilde{\mathbf{x}}_i^g, \tilde{y}_i^g) \in D_s^g, CE(f_t(\tilde{\mathbf{x}}_i^g), \tilde{y}_i^g) \leq \alpha(\rho, \tilde{y}_i^g), i = 1, \dots, M^g\} & \text{for classification} \\ \{(\tilde{\mathbf{x}}_i^g, \tilde{y}_i^g) \mid (\tilde{\mathbf{x}}_i^g, \tilde{y}_i^g) \in D_s^g, |f_t(\tilde{\mathbf{x}}_i^g) - \tilde{y}_i^g| \leq \alpha(\rho), i = 1, \dots, M^g\} & \text{for regression} \end{cases},$$

and

$$\hat{D}_\rho^g = \left\{ (\tilde{\mathbf{x}}_i^g, \hat{y}_i^g) \mid (\tilde{\mathbf{x}}_i^g, \tilde{y}_i^g) \in \tilde{D}_\rho^g, \hat{y}_i^g = f_t(\tilde{\mathbf{x}}_i^g), i = 1, \dots, M^g \right\},$$

where $CE(\cdot, \cdot)$ is the cross entropy loss, and α is a cut-off point defined in Section 3.4 and related to a positive hyper-parameter ρ or a class label \tilde{y}_i^g . The variables in the parenthesis of α (i.e., ρ and \tilde{y}_i^g) specify which quantity affects α . The processed samples D_ρ^g are then used to augment the training set D^r . Finally, **M3** trains the student model f_s on the augmented training set $D^r \cup D_\rho^g$. The student model trained on $D^r \cup D_\rho^g$ is expected to perform better than the one trained on D^r . More details of the three modules are described in Sections 3.3 to 3.5 and the evolution of fake sample datasets is shown in Fig. S.4.13 in Supp. S.4. Some visual illustrations and an ablation study of **M1**, **M2** and **M3** are also provided in Section 5.3.

3.3. **M1**: Drop low-quality fake samples via subsampling

Since low-quality samples may reduce prediction accuracy if they are used to augment the training set, **M1** (*subsampling*) is adopted to drop these samples. The subsampling module implements cDR-RS (Ding et al., 2022) which performs rejection sampling to accept or reject a fake image-label pair (\mathbf{x}^g, y^g) in terms of the density ratio of \mathbf{x}^g conditioning on y^g . Ding et al. (2022) shows that cDR-RS can effectively improve the

overall image quality of both class-conditional GANs and CcGANs in the conditional image synthesis setting. Thus, cDR-RS is very suitable for dropping low-quality samples in the proposed cGAN-KD framework.

3.4. M2: Distill knowledge via label adjustment

Assume that we have a fake image-label pair $(\tilde{x}^g, \tilde{y}^g)$ generated from the previous module **M1**. The label \tilde{y}^g is called the *assigned label* of \tilde{x}^g in this paper. Please note that the assigned label \tilde{y}^g may deviate from the *actual label* of \tilde{x}^g (aka *label inconsistency*) because of the imperfectness of cGAN’s training and density ratio estimation. For example, CcGANs (Ding et al., 2021a,b) can generate many fake facial images conditional on age 3, but some of them may actually come from the population of age 5. Besides the assigned and actual label, there is a third type of label for \tilde{x}^g called *predicted label*. The predicted label denoted by \hat{y}^g is defined as the prediction from the teacher model f_t on \tilde{x}^g , i.e., $\hat{y}^g = f_t(\tilde{x}^g)$. The predicted label is assumed to be closer to the actual label than the assigned label, because discriminative learning (i.e., fitting f_t) is often easier than generative learning (i.e., fitting cGANs). Based on the assigned and predicted labels of N^g fake images generated from the previous module **M1**, the two-stage module **M2** primarily aims to increase the label consistency of fake image-label pairs. **After applying M2, the relation between images and labels (“knowledge”) learned by the teacher model f_t is stored in the processed fake samples D_ρ^g .** Additionally, **M2** may also drop some unrealistic images so the overall visual quality can be further improved.

More specifically, **M2** includes two sequential sub-modules, a *filtering* sub-module and a *replacement* sub-module. The replacement sub-module is enabled only for regression problems. These two sub-modules are introduced as follows: **(1)** The *filtering* sub-module computes the errors between assigned and predicted labels, and drops fake samples with errors larger than a cut-off point α . Here, the errors are defined as the cross entropy (CE) loss for classification and mean absolute error (MAE) for regression. Two corresponding algorithms for classification and regression are summarized in Algorithm 1 and Algorithm 2, respectively. The filtering threshold α equals the ρ -th quantile of fake samples’ errors. A smaller ρ implies that more samples are dropped. For classification, we compute one α for each class and conduct the filtering within each class. Differently, we have a global α to filter fake images with different labels in regression tasks. As for the selection of $\rho \in [0, 1]$, we empirically suggest $\rho = 0.9$ for classification and $\rho = 0.7$ for regression. We recommend a smaller ρ for regression because the label inconsistency problem is more severe for CcGANs than class-conditional GANs. After removing fake samples with large errors, the label consistency of the fake samples can be improved. Additionally, our empirical study also shows that a significant error between the assigned and predicted labels often implies poor visual quality of the corresponding fake images. Consequently, as a side effect, the filtering sub-module can also help improve the overall visual quality of fake images. **(2)** The subsequent *replacement* sub-module is enabled for regression only. Similar to pseudo-labeling (Lee et al., 2013; Arazo et al., 2020) in semi-supervised learning, it *replaces* the assigned label \tilde{y}^g with the predicted label \hat{y}^g . As shown in Ding et al. (2021a,b), CcGANs often suffer from the label inconsistency problem, and the replacement sub-module can effectively alleviate this problem. This sub-module is not necessary for classification because most label-inconsistent samples have already been dropped after filtering.

Algorithm 1: A filtering algorithm for classification with C classes in **M2** with a hyper-parameter ρ to adjust class labels and drop low-quality samples. We suggest $\rho = 0.9$ for classification. Please note that, in classification, we calculate one filtering threshold $\alpha(\rho, c)$ per class and we conduct filtering within each class.

```

1 for  $c$  from 1 to  $C$  do
2   Sample  $N^g/C$  fake images from a trained cGAN via cDR-RS conditional on class  $c$ ;
3   Predict the labels of these fake images by the pre-trained teacher model  $f_t$ ;
4   Compute the cross entropy (CE) loss between the assigned and predicted labels. Note that, we use soft
   predicted labels (refer to Figure 1) to compute the error.;
5   Sort these errors from smallest to largest and the  $\rho$ -th quantile of these errors is set as the filtering threshold (i.e.,
   the cut-off point  $\alpha(\rho, c)$ );
6   Remove fake images pairs with errors larger than the filtering threshold  $\alpha(\rho, c)$ ;
7 end

```

Algorithm 2: A filtering algorithm for regression in **M2** with a hyper-parameter ρ to adjust regression labels and drop low-quality samples. We suggest $\rho = 0.7$ for regression. Unlike classification, in regression, we calculate a global filtering threshold $\alpha(\rho)$ to filter fake images with different labels.

- 1 Sample N^g fake image-label pairs from a trained cGAN with cDR-RS;
 - 2 Predict the labels of these fake images by the pre-trained teacher model f_t ;
 - 3 Compute the **mean absolute error (MAE)** between the assigned and predicted labels. ;
 - 4 Sort these errors from smallest to largest and the ρ -th quantile of these errors is set as the filtering threshold (i.e., the cut-off point $\alpha(\rho)$) ;
 - 5 Remove fake image-label pairs with errors larger than the filtering threshold $\alpha(\rho)$.
-

3.5. **M3**: Transfer knowledge via data augmentation

The processed fake samples D_ρ^g from the previous module are used to augment the original training set D^r , i.e., to give $D^r \cup D_\rho^g$. To transfer knowledge distilled from the pre-trained f_t , we train f_s on the augmented dataset in **M3**. Please note that empirical studies in Section 5 show that as M^g increases, the test error of f_s often does not stop decreasing until M^g is larger than a certain threshold and then starts fluctuating over a small range. Since it is hard to obtain the optimal M^g in practice and a hefty M^g usually does not cause a significant adverse effect on precision, we suggest generating the maximum number of processed samples allowed by the computational budget. Two intuitive explanations for the effectiveness of such data augmentation are shown as follows:

- As shown in Figs. 10 to 14 of Brock et al. (2019), cGANs such as BigGAN can generate fake images that are unseen in the training set. In other words, cGANs may yield new information which may help improve the student’s generalization performance.
- Although cGANs may yield new information, the fake images from cGANs may be inconsistent with their assigned labels. We use the accurate teacher model to adjust the fake images’ labels, so the image-label relation (“knowledge”) learned by the teacher is stored in the fake samples. This learned knowledge is transferred to the student model via data augmentation.

Note that **M3** makes our method fundamentally different from many existing KD methods (Hinton et al., 2015; Mirzadeh et al., 2020; Romero et al., 2015; Zagoruyko & Komodakis, 2017; Tung & Mori, 2019; Ahn et al., 2019; Park et al., 2019; Passalis & Tefas, 2018; Heo et al., 2019; Kim et al., 2018; Tian et al., 2019; Xu et al., 2020; Chen et al., 2021b,a; Wang et al., 2022; Chen et al., 2022), because the distilled knowledge is transferred through samples instead of specially designed loss functions or training tasks. **M3** is also distinct from existing GAN-based data augmentation methods (Frid-Adar et al., 2018; Sixt et al., 2018; Wu et al., 2018; Zhu et al., 2018; Mariani et al., 2018), because these methods do not filter out unrealistic images or adjust the labels of label-inconsistent images. Consequently, these low-quality samples may cause negative effects on the supervised learning tasks, making these GAN-based data augmentation methods unstable.

3.6. Advantages of cGAN-KD

3.6.1. A unified knowledge distillation framework for image classification and regression

As the main advantage of cGAN-KD, all necessary steps in the workflow of cGAN-KD are applicable to both classification and regression (with a scalar response). Although some feature-based KD methods (e.g., FitNet (Romero et al., 2015), AT (Zagoruyko & Komodakis, 2017), and RKD (Park et al., 2019)) may be adjusted to fit the regression task by removing their logit-related components, empirical studies in Section 5.2 show that such modification fails to result in stable performance, and it sometimes even makes students perform worse. Furthermore, the theoretical analysis of cGAN-KD (see Section 4) also has the same general formulation for both tasks. Thus, cGAN-KD is actually a unified KD framework.

3.6.2. Compatibility with state-of-the-art KD methods

cGAN-KD distills and transfers knowledge via fake samples, and it does not require extra loss functions or network architecture changes. Thus, cGAN-KD can be combined with many state-of-the-art KD methods for image classification to improve their performance. To embed a state-of-the-art KD method into cGAN-KD,

we just need to train the student model on the augmented training set with this KD method in **M3** but keep other procedures in Figure 3 unchanged.

3.6.3. Architecture-invariance

As shown by our experiments in Section 5 and some papers (Mirzadeh et al., 2020; Xu et al., 2020), the architecture differences between a teacher model and a student model may influence the performance of some existing KD methods because these methods rely on logits or intermediate layers to transfer knowledge. Other KD methods such as SSKD (Xu et al., 2020) and SimKD (Chen et al., 2022) even require some adjustments to the teacher and student models' architectures. Conversely, since the proposed cGAN-KD framework distills and transfers knowledge via fake samples, there are no restrictions on the teacher and student models' architectures. The theoretical analysis in Section 4 also tells us to choose the most accurate teacher model for the label adjustment without worrying about the architecture differences, making cGAN-KD more flexible than other KD methods.

4. Error bound of cGAN-KD

This section derives an error bound of cGAN-KD, reflecting the distance of a student model trained by cGAN-KD from the theoretically optimal predictor. This theoretical analysis illustrates how the cGAN-KD framework improves the precision of f_s , and it also helps guide our implementation of cGAN-KD in practice.

Before we move to the theoretical analysis, we first introduce some notations. Denote by $p_g(\mathbf{x}, y)$ the density function of the distribution of unprocessed fake samples. Denote by $p_g^s(\mathbf{x}, y)$ and $p_g^o(\mathbf{x}, y)$ the density functions of the distributions of fake samples that are processed by **M1** and **M2** respectively. The evolution of fake data and their distributions is visualized in Fig. S.4.13.. Additionally, we denote the augmented training dataset in **M3** as D_{aug} , i.e., $D_{\text{aug}} := D^r \cup D_\rho^g$. Then, we define a theoretical loss of a predictor f and its empirical approximation based on D_{aug} ,

$$\begin{aligned}\mathcal{V}(f) &:= \mathbb{E}_{(\mathbf{x}, y) \sim p_r(\mathbf{x}, y)} [\mathcal{L}(f(\mathbf{x}), y)], \\ \widehat{\mathcal{V}}(f) &:= \frac{1}{N^r + M^g} \sum_{(\mathbf{x}_i, y_i) \in D_{\text{aug}}} \mathcal{L}(f(\mathbf{x}_i), y_i),\end{aligned}$$

where \mathcal{L} is either the CE loss for classification or the SE loss for regression. Without loss of generality, we assume $y \in [0, 1]$ in regression tasks. Let f^* be the *optimal predictor* which minimizes $\mathcal{V}(f)$. We denote by \mathcal{F}_s the *hypothesis space* of f_s , i.e., a set of functions that can be represented by f_s . Note that \mathcal{F}_s may not include f^* . Then, we define f_s° and \hat{f}_s as

$$f_s^\circ = \arg \min_{f_s \in \mathcal{F}_s} \mathcal{V}(f_s), \quad \hat{f}_s = \arg \min_{f_s \in \mathcal{F}_s} \widehat{\mathcal{V}}(f_s).$$

If the architecture of the student model f_s is determined, then the hypothesis space \mathcal{F}_s is fixed. This hypothesis space may not cover the theoretically optimal predictor f^* . In this case, the training of the student model aims to minimize $\mathcal{V}(f_s)$ with respect to $f_s \in \mathcal{F}_s$, i.e., to get f_s° . Unfortunately, obtaining f_s° is also inaccessible because the density function $p_r(\mathbf{x}, y)$ is unknown and the expectation in $\mathcal{V}(f_s)$ is intractable. In the cGAN-KD framework, we approximate $\mathcal{V}(f_s)$ by $\widehat{\mathcal{V}}(f_s)$, and the minimizer we actually get in practice is \hat{f}_s . Therefore, **we are interested in how far \hat{f}_s deviates from f^*** . We characterize this error via the theoretical loss $\mathcal{V}(f)$, i.e., $\mathcal{V}(\hat{f}_s) - \mathcal{V}(f^*)$. If $\hat{f}_s = f^*$, this error equals zero. An illustrative figure for this error is shown in Fig. 4. Instead of providing an analytical form of this error, we derive its upper bound (i.e., error bound) in the form of a concentration inequality (refer to Theorem 1).

Theorem 1 (Error Bound). *Suppose that*

- A1.** *(i.i.d. samples) $D^r \stackrel{i.i.d.}{\sim} p_r(\mathbf{x}, y)$, $D_\rho^g \stackrel{i.i.d.}{\sim} p_g^o(\mathbf{x}, y)$, and the augmented dataset is considered as i.i.d. samples from a mixture distribution, i.e.,*

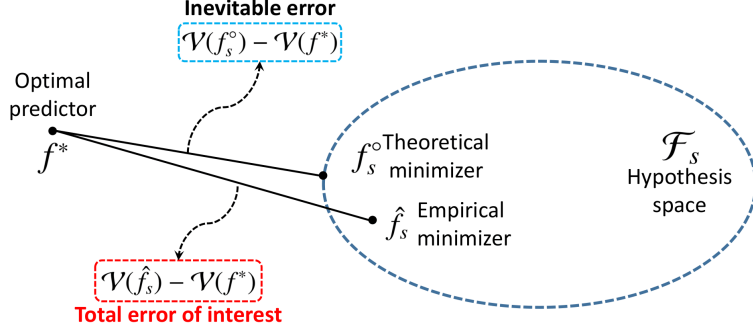


Fig. 4: **An illustration of the error bound of cGAN-KD.** \hat{f}_s is the minimizer we can obtain in practice, and we are interested in how far it deviates from the optimal predictor f^* , i.e., $\mathcal{V}(\hat{f}_s) - \mathcal{V}(f^*)$. We derive an upper bound of $\mathcal{V}(\hat{f}_s) - \mathcal{V}(f^*)$ in Theorem 1. Please note that $\mathcal{V}(f_s^\circ) - \mathcal{V}(f^*)$ is an inevitable error, because the hypothesis space may not cover f^* .

$$D_{aug} \stackrel{i.i.d.}{\sim} \theta p_r(\mathbf{x}, y) + (1 - \theta) p_g^\theta(\mathbf{x}, y) =: p_\theta(\mathbf{x}, y), \quad (5)$$

where $\theta \in [0, 1]$.

A2. (Measurability) f_s is measurable for all $f_s \in \mathcal{F}_s$.

A3. (Distribution gap) There is a constant $C_{M1} > 0$ such that

$$TV(p_r, p_g^\theta) = C_{M1} + \Theta(\mathbb{E}_{(\mathbf{x}, y) \sim p_r(\mathbf{x}, y)} [\mathcal{L}(f_t(\mathbf{x}), y)]), \quad (6)$$

where TV denotes the total variation distance (Gibbs & Su, 2002) between the probability distributions of real samples and processed fake samples (with density functions $p_r(\mathbf{x}, y)$ and $p_g^\theta(\mathbf{x}, y)$ respectively); and $f(x) = \Theta(g(x))$ means $f(x) = O(g(x))$ and $g(x) = O(f(x))$.

A4. (Boundedness) There exists a constant $0 < C_{\mathcal{L}} < +\infty$, such that $\forall(\mathbf{x}, y)$, $\mathcal{L}(f_s(\mathbf{x}), y) \leq C_{\mathcal{L}}$.

Then, $\forall \delta \in (0, 1)$, with probability at least $1 - \delta$,

$$\begin{aligned} & \mathcal{V}(\hat{f}_s) - \mathcal{V}(f^*) \\ & \leq 4C_{\mathcal{L}} \widehat{\mathcal{R}}_{N^r + M^g}(\mathcal{F}_s) + 2C_{\mathcal{L}} \sqrt{\frac{4}{N^r + M^g} \log\left(\frac{2}{\delta}\right)} \\ & \quad + 4C_{\mathcal{L}}(1 - \theta) (C_{M1} + \Theta(\mathbb{E}_{(\mathbf{x}, y) \sim p_r(\mathbf{x}, y)} [\mathcal{L}(f_t(\mathbf{x}), y)])) \\ & \quad + (\mathcal{V}(f_s^\circ) - \mathcal{V}(f^*)), \end{aligned} \quad (7)$$

where $\widehat{\mathcal{R}}_{N^r + M^g}(\mathcal{F}_s)$ stands for the empirical Rademacher complexity (Mohri et al., 2018, Definition 3.1) of \mathcal{F}_s , which is defined on $N^r + M^g$ samples independently drawn from p_θ .

Proof. The proof is in Supp. S.3. □

Remark 1 (Rationale for **A3** and **A4**). In the cGAN-KD framework, processed fake images are used to augment the training set, so the distribution gap between $p_r(\mathbf{x}, y)$ and $p_g^\theta(\mathbf{x}, y)$ (measured by the total variation distance) should have a significant impact on the student model's performance. Thus, in **A3** of Theorem 1, we model the distribution gap by the summation of two components. The first component C_{M1} stands for the divergence caused by the trained cGAN and the subsampling module. The second component is controlled by the generalization performance of f_t —the expected loss of the trained teacher model over the true data distribution.

It is also worth discussing the rationale for **A4**. The two types of learning tasks considered in this work are the regression and classification, for which we use the squared loss $(f_s(\mathbf{x}) - y)^2$ and the cross entropy loss

$\sum_{c=1}^C \{-y_c \log p_c^s\}$ respectively. Take the regression task first. In our experiments on the regression datasets, the last layer of $f_s(\mathbf{x})$ is the ReLU activation function (Fukushima, 1969; Fukushima & Miyake, 1982), so $f_s(\mathbf{x}) \geq 0$. Since $y \in (0, 1)$, as long as $f_s(\mathbf{x})$ is not an unstable predictor, it should not output arbitrarily large values, which implies $f_s(\mathbf{x})$ can be bounded by a positive constant. Therefore, the squared loss is bounded and **A4** is satisfied. For the classification task, a sufficient condition to **A4** is that $p_c^s \geq \epsilon > 0$ when $y_c = 1$, representing that our classifier cannot produce 0 probability for the true label, which is reasonable in practice.

Remark 2 (Illustration of Theorem 1). The four terms on the right side of Eq. (7) show that the error of f_s has four components, and reducing them can improve the performance of f_s . The first and last terms are only relevant to the nature of f_s , so they are not influenced by f_t . If f_s does not output arbitrarily extreme predictions (as discussed in Remark 1), $C_{\mathcal{L}}$ stays at a moderate level, implying the first term is also small. The last term is inevitable because \mathcal{F}_s may not include f^* . The second term diminishes if we set M^g large. For the third term, $\theta \rightarrow 0$ as M^g increases. Then, the third term is only controlled by the properties of \mathcal{L} and the distribution gap. To reduce the distribution gap, we can either improve the cGAN model and the subsampling method, or choose f_t to have better generalization performance.

Therefore, Theorem 1 implies when implementing cGAN-KD we should

- use state-of-the-art cGANs and subsampling methods;
- set M^g large;
- choose a teacher f_t with the highest precision as possible.

5. Experiments

This section aims to experimentally demonstrate the effectiveness of the proposed cGAN-KD framework in image classification and regression (with a scalar response) tasks. We conduct extensive experiments on four image datasets: CIFAR-100 (Krizhevsky et al., 2009) and ImageNet-100 (Cao et al., 2017) for image classification; and Steering Angle (Chen, 2018b,a) and UTKFace (Zhang et al., 2017) for image regression. We compare the cGAN-KD framework against different types of KD methods on CIFAR-100 and ImageNet-100 (Section 5.1). Since the logits of teachers and students are unavailable in regression tasks, we only show the effectiveness of the cGAN-KD framework over some modified feature-based KD methods on Steering Angle and UTKFace (Section 5.2). In addition to these experiments, we conduct an ablation study to test the effects of different (sub-)modules in the cGAN-KD framework (Section 5.3). Finally, some additional analyses about hyper-parameters, selection of teacher models, and running time and memory cost are also provided in Section 5.4. Please note that for image regression, as suggested by Ding et al. (2021a,b), when training CcGANs, f_t , and f_s , regression labels are normalized to real numbers in $[0, 1]$. Nevertheless, in the evaluation stage of f_t and f_s , we compute *mean absolute error* (MAE) on unnormalized regression labels.

5.1. Classification: CIFAR-100 and ImageNet-100

5.1.1. Datasets

For classification, we conduct experiments on two datasets: CIFAR-100 and ImageNet-100. CIFAR-100 consists of 60,000 RGB images at 32×32 resolution uniformly spread across 100 classes. The overall number of training samples is 50,000 (500 for each class), and the remaining 10,000 samples (100 for each class) are for testing. ImageNet-100, as a subset of ImageNet (Deng et al., 2009), has 128,503 RGB images at 128×128 resolution from 100 classes. In our experiment, we randomly split ImageNet-100 into a training set and a test set, where 10,000 images are for testing (on average 100 images per class) and the rest are for training.

5.1.2. The selection of teachers and students

To select students and teachers for this experiment, some popular classifiers are trained from scratch on each dataset, and their Top-1 test accuracies are shown in Tables S.5.8 and S.6.11 in Appendix. Some light-weight neural networks (shown in Table 2 and Table 3) with low test accuracies are chosen as student models, and we aim to improve their performance. Some neural networks with high accuracies are chosen as the teacher models for the filtering step in cGAN-KD and other compared KD methods.

5.1.3. Compared methods and implementation details

Compared KD methods for classification tasks are NOKD (i.e., no KD method is applied), BLKD (Hinton et al., 2015), FitNet (Romero et al., 2015), AT (Zagoruyko & Komodakis, 2017), PKT (Passalis & Tefas, 2018), FT (Kim et al., 2018), SP (Tung & Mori, 2019), VID (Ahn et al., 2019), RKD (Park et al., 2019), AB (Heo et al., 2019), CRD (Tian et al., 2019), TAKD (Mirzadeh et al., 2020), SSKD (Xu et al., 2020), ReviewKD (Chen et al., 2021b), SemCKD (Chen et al., 2021a; Wang et al., 2022), SimKD (Chen et al., 2022), and the proposed cGAN-KD framework (including incorporating other KD methods into cGAN-KD, which is denoted by cGAN-KD + X).

On CIFAR-100, we implement BLKD, FitNet, AT, PKT, FT, SP, VID, RKD, AB, and CRD via `RepDistiller` (a GitHub repository provided by Tian et al. (2019)). ReviewKD, SemCKD, SimKD, and SSKD are implemented based on their official implementations. We implement TAKD based the provided algorithm in Mirzadeh et al. (2020), where $\lambda_{KD} = 0.5$ and $T = 5$ (Ruffy & Chahal, 2019). Note that most of these KD methods do not support DenseNet (Huang et al., 2017) as the teacher due to its densely connection, but cGAN-KD and BLKD still work well. For ImageNet-100, compared with the CIFAR-100 experiment, we test fewer KD methods and teacher-student pairs due to limited computational resources.

To implement the proposed cGAN-KD framework, we train two BigGAN models (Brock et al., 2019) for CIFAR-100 and ImageNet-100, respectively. DiffAugment (Zhao et al., 2020b) is also incorporated into the BigGAN training to improve the training stability. DenseNet121 and DenseNet161 (Huang et al., 2017) are chosen as the teacher models for filtering when implementing cGAN-KD due to their highest precision on CIFAR-100 and ImageNet-100, respectively. As we suggested in Section 3.4, we let $\rho = 0.9$ on both datasets. We generate $M^g = 100,000$ processed fake samples for each dataset. Please note that we only combine cGAN-KD with six representative KD methods (i.e., BLKD, FitNet, VID, RKD, CRD, and SSKD) due to limited computational resources. When combining cGAN-KD with chosen KD methods (e.g., cGAN-KD+BLKD in Table 2), we have two types of teacher models: *the primary teacher* and *the secondary teacher*. The primary teacher is for filtering in cGAN-KD which is fixed as DenseNet121 (for CIFAR-100) or DenseNet161 (ImageNet-100), and the secondary teacher is for the implementation of existing KD methods.

All results of the CIFAR-100 experiment are reported in mean (standard deviation) **over 4 repetitions**. Differently, all results of the ImageNet-100 experiment are reported in **a single trial**. Other implementation details such as learning rate, batch size, weight decay, number of epochs, seed, and optimizer are shown in Sections S.5 and S.6 in Appendix.

5.1.4. Experimental results

For CIFAR-100, Tables 2 and 3 show that among 21 teacher-student pairs, cGAN-KD-based methods perform the best in 18 pairs. For ImageNet-100, Table 4 shows that cGAN-KD+SSKD beats all compared methods in all teacher-student pairs.

From these results, we can see that cGAN-KD alone can effectively improve all students’ performance on both classification datasets (i.e., cGAN-KD versus NOKD); however, we highly recommend combining it with other existing KD methods, e.g., cGAN-KD+BLKD and cGAN-KD+SSKD. In Table 4, after being combined with cGAN-KD, BLKD performs comparably to or even better than the state-of-the-art SSKD on ImageNet-100. Notably, incorporating cGAN-KD into training improves the state-of-the-art SSKD by an average of 1.32% in test accuracy on ImageNet-100 across five teacher-student pairs.

Please note that, as one of the recently proposed KD methods, ReviewKD requires that teacher and student network architectures have the same number of stages, and the feature map dimensions of teacher and student at each stage are consistent. Unfortunately, many teacher-student combinations in our experiment don’t satisfy this requirement. Consequently, these teacher-student pairs are not supported by ReviewKD, and their corresponding results are marked by NA. Furthermore, although SimKD performs the best in 3 teacher-student pairs on CIFAR-100, it causes negative effects on some students’ performance when teachers are ResNet110 and ResNet50 (marked in red), implying its instability. Additionally, SemCKD does not converge when teacher and student are ResNet110 and ResNet20, so the corresponding results are marked by NA. In many teacher-student pairs, SemCKD is able to beat other feature-based methods, but it fails to outperform SSKD. In fact, our extensive experiments show that, among many existing KD methods, SSKD is the most effective and stable one.

Table 2: **CIFAR-100: Average Top-1 test accuracy (%) of compared KD methods (KD between similar architectures) with standard deviation after the “±” symbol. Bold and underline denote the best and the second best results, respectively.**

Teacher	ResNet110 (73.27)	ResNet32x4 (79.11)	VGG13 (74.85)	VGG19 (73.88)	WRN40×2 (75.82)	ResNet32x4 (79.11)
Student	ResNet20	ResNet20	VGG8	VGG8	WRN40×1	ResNet8x4
NOKD	69.22 ± 0.39	69.22 ± 0.39	70.61 ± 0.44	70.61 ± 0.44	71.40 ± 0.11	72.74 ± 0.07
BLKD (2015)	70.44 ± 0.26	69.15 ± 0.33	72.93 ± 0.19	72.03 ± 0.19	73.45 ± 0.19	73.44 ± 0.29
FitNet (2015)	69.99 ± 0.19	70.03 ± 0.27	73.46 ± 0.27	71.96 ± 0.09	74.09 ± 0.21	74.96 ± 0.06
AT (2017)	70.95 ± 0.29	70.13 ± 0.43	73.44 ± 0.18	71.11 ± 0.21	74.12 ± 0.25	74.88 ± 0.26
PKT (2018)	70.91 ± 0.08	69.74 ± 0.30	73.60 ± 0.37	72.45 ± 0.20	73.87 ± 0.46	74.48 ± 0.26
FT (2018)	70.97 ± 0.14	70.23 ± 0.19	73.14 ± 0.36	72.09 ± 0.20	73.88 ± 0.23	74.88 ± 0.19
SP (2019)	70.56 ± 0.06	69.39 ± 0.36	73.33 ± 0.12	71.72 ± 0.22	73.81 ± 0.11	73.92 ± 0.22
VID (2019)	70.71 ± 0.18	69.86 ± 0.20	73.44 ± 0.30	72.19 ± 0.15	73.80 ± 0.28	74.53 ± 0.16
RKD (2019)	70.61 ± 0.35	69.46 ± 0.25	73.34 ± 0.36	71.79 ± 0.27	73.66 ± 0.26	74.06 ± 0.15
AB (2019)	70.48 ± 0.23	69.91 ± 0.14	73.26 ± 0.26	71.73 ± 0.29	74.19 ± 0.12	74.47 ± 0.16
CRD (2019)	71.39 ± 0.17	70.41 ± 0.16	73.88 ± 0.26	72.59 ± 0.13	74.33 ± 0.37	75.25 ± 0.16
TAKD (2020)	70.75 ± 0.32	69.74 ± 0.42	73.23 ± 0.31	71.73 ± 0.24	74.49 ± 0.28	73.47 ± 0.32
SSKD (2020)	70.92 ± 0.20	71.10 ± 0.24	74.52 ± 0.23	73.27 ± 0.17	75.56 ± 0.25	75.70 ± 0.17
ReviewKD (2021)	70.97 ± 0.11	NA	74.00 ± 0.13	72.84 ± 0.42	75.27 ± 0.11	75.55 ± 0.27
SemCKD (2021)	NA	70.16 ± 0.47	74.01 ± 0.17	73.13 ± 0.09	73.87 ± 0.14	75.62 ± 0.22
SimKD (2022)	68.94 ± 0.32	72.33 ± 0.13	74.51 ± 0.14	73.28 ± 0.24	75.56 ± 0.09	77.28 ± 1.08
cGAN-KD	70.71 ± 0.10	70.71 ± 0.10	72.08 ± 0.21	72.08 ± 0.21	73.19 ± 0.48	72.90 ± 0.11
cGAN-KD + BLKD	71.30 ± 0.34	70.73 ± 0.12	74.49 ± 0.13	73.74 ± 0.15	75.22 ± 0.14	73.71 ± 0.25
cGAN-KD + FitNet	70.66 ± 0.30	71.30 ± 0.36	74.62 ± 0.09	<u>73.92 ± 0.37</u>	75.41 ± 0.19	74.36 ± 0.25
cGAN-KD + VID	70.80 ± 0.24	71.25 ± 0.17	74.81 ± 0.07	73.89 ± 0.15	75.07 ± 0.26	74.59 ± 0.24
cGAN-KD + RKD	<u>71.63 ± 0.06</u>	71.08 ± 0.28	74.62 ± 0.21	73.60 ± 0.12	75.50 ± 0.18	74.22 ± 0.21
cGAN-KD + CRD	72.24 ± 0.11	71.75 ± 0.19	75.05 ± 0.14	74.07 ± 0.08	75.98 ± 0.29	75.53 ± 0.11
cGAN-KD + SSKD	71.26 ± 0.26	72.29 ± 0.23	74.91 ± 0.09	73.59 ± 0.21	75.71 ± 0.19	76.65 ± 0.16

5.2. Regression: Steering Angle and UTKFace

5.2.1. Datasets

This experiment is conducted on the Steering Angle and UTKFace datasets to show that cGAN-KD also performs very well in the image regression tasks with a scalar response variable. Steering Angle, a subset of an autonomous driving dataset (Chen, 2018b,a), includes 12,508 RGB images at 64×64 resolution with 1,773 distinct steering angles in $[-88.13^\circ, 97.92^\circ]$ as labels. We split the range of angles into 246 disjoint unequal intervals, where each interval should have at least 40 instances. In each interval, 80% instances are randomly selected for training, and the rest are for testing. UTKFace is an RGB human face image dataset with ages as regression labels. We use the processed UTKFace dataset (Ding et al., 2021b,a), which consists of 14,760 RGB images with ages in $[1, 60]$. The number of images ranges from 50 to 1051 for different ages, and all images are of size 64×64 . Among these images, 80% are randomly selected for training for each age, and the rest are held out for testing.

5.2.2. The selection of teachers and students

Similar to classification, to select student and teacher models for this experiment, some popular neural networks are trained from scratch on each dataset, and their *mean absolute errors* (MAE) on test sets are shown in Tables S.7.13 and S.8.15 in Appendix. Some light-weight neural networks (shown in Table 5) with high test MAE are chosen as student models, and we aim to improve their accuracies. VGG19 and VGG11 (Simonyan & Zisserman, 2014) are chosen as the teacher models for the label adjustment module in cGAN-KD on Steering Angle and UTKFace, respectively.

5.2.3. Compared methods and implementation details

Note that there is no general KD method for image regression tasks with a scalar response. Thus, we compare cGAN-KD against modified FitNet, AT, and RKD, where we exclude any logit-related terms from the loss functions of these three feature-based KD methods. Compared KD methods in regression tasks include NOKD, FitNet, AT, RKD, cGAN-KD, and cGAN-KD + FitNet. Similar to our classification experiment, we implement FitNet, AT, and RKD by `RepDistiller` (a GitHub repository provided by Tian et al. (2019)).

Table 3: **CIFAR-100: Average Top-1 test accuracy (%) of compared KD methods (KD between different architectures) with standard deviation after the “±” symbol. Bold and underline denote the best and the second best results, respectively.**

Teacher	WRN40×2 (75.82)	WRN40×2 (75.82)	ResNet32x4 (79.11)	ResNet32x4 (79.11)	ResNet32x4 (79.11)	ResNet32x4 (79.11)	ResNet50 (79.51)	ResNet50 (79.51)	ResNet50 (79.51)
Student	MobileNetV2	VGG8	MobileNetV2	VGG8	ShuffleNetV1	ShuffleNetV2	MobileNetV2	VGG8	ShuffleNetV1
NOKD	64.59 ± 0.34	70.61 ± 0.44	64.59 ± 0.34	70.61 ± 0.44	71.47 ± 0.28	72.63 ± 0.49	64.59 ± 0.34	70.61 ± 0.44	71.47 ± 0.28
BLKD (2015)	68.31 ± 0.21	73.38 ± 0.15	67.19 ± 0.39	72.57 ± 0.21	74.17 ± 0.15	74.76 ± 0.12	67.61 ± 0.89	73.52 ± 0.21	75.19 ± 0.33
FitNet (2015)	68.63 ± 0.15	73.46 ± 0.11	67.57 ± 0.28	73.47 ± 0.22	75.73 ± 0.43	76.64 ± 0.34	67.41 ± 0.92	72.97 ± 0.32	75.16 ± 0.40
AT (2017)	68.76 ± 0.11	73.22 ± 0.34	67.03 ± 0.24	72.06 ± 0.42	75.79 ± 0.18	75.98 ± 0.21	65.97 ± 0.42	73.83 ± 0.19	75.80 ± 0.22
PKT (2018)	68.64 ± 0.43	73.70 ± 0.26	68.00 ± 0.26	72.86 ± 0.21	74.88 ± 0.23	75.52 ± 0.17	67.92 ± 0.87	73.61 ± 0.23	75.59 ± 0.17
FT (2018)	67.32 ± 3.99	73.56 ± 0.25	64.61 ± 0.33	72.83 ± 0.14	75.48 ± 0.22	76.16 ± 0.42	67.92 ± 0.22	73.00 ± 0.08	76.03 ± 0.24
SP (2019)	67.77 ± 0.65	73.40 ± 0.14	67.33 ± 0.50	72.94 ± 0.34	75.28 ± 0.11	75.95 ± 0.38	68.55 ± 0.30	73.58 ± 0.18	76.11 ± 0.23
VID (2019)	67.54 ± 0.47	74.00 ± 0.13	66.80 ± 0.59	72.84 ± 0.29	75.36 ± 0.20	75.62 ± 0.18	68.42 ± 0.37	73.48 ± 0.05	75.43 ± 0.29
RKD (2019)	67.77 ± 0.77	73.36 ± 0.20	67.22 ± 0.19	72.22 ± 0.13	74.66 ± 0.16	75.36 ± 0.38	67.72 ± 0.65	73.39 ± 0.23	75.50 ± 0.38
AB (2019)	NA	NA	NA	NA	75.38 ± 0.48	76.00 ± 0.05	68.66 ± 0.67	73.50 ± 0.20	NA
CRD (2019)	70.92 ± 1.70	74.53 ± 0.41	69.02 ± 0.25	73.90 ± 0.19	75.25 ± 0.31	76.06 ± 0.20	69.59 ± 0.68	74.42 ± 0.06	76.26 ± 0.36
TAKD (2020)	68.67 ± 0.43	73.85 ± 0.12	67.29 ± 0.36	72.62 ± 0.22	74.41 ± 0.29	74.86 ± 0.03	68.37 ± 0.47	73.43 ± 0.17	75.14 ± 0.06
SSKD (2020)	71.57 ± 0.13	75.30 ± 0.16	69.94 ± 1.88	75.48 ± 0.21	77.88 ± 0.13	78.47 ± 0.09	71.86 ± 0.30	75.48 ± 0.10	77.87 ± 0.22
ReviewKD (2021)	NA	NA	NA	NA	76.78 ± 0.45	77.14 ± 0.32	66.35 ± 0.25	NA	NA
SemCKD (2021)	69.30 ± 0.25	74.48 ± 0.08	68.56 ± 0.37	74.83 ± 0.31	76.56 ± 0.12	77.50 ± 0.22	67.62 ± 0.54	73.80 ± 0.33	75.77 ± 0.26
SimKD (2022)	69.76 ± 0.18	75.98 ± 0.16	68.31 ± 0.18	<u>75.61 ± 0.11</u>	75.88 ± 2.40	77.68 ± 0.20	63.48 ± 0.14	66.97 ± 0.24	65.47 ± 0.12
cGAN-KD	68.35 ± 0.22	72.08 ± 0.21	68.35 ± 0.22	72.08 ± 0.21	74.60 ± 0.48	75.22 ± 0.43	68.35 ± 0.22	72.08 ± 0.21	74.60 ± 0.48
cGAN-KD + BLKD	70.03 ± 0.35	74.51 ± 0.12	69.66 ± 0.20	74.33 ± 0.21	76.17 ± 0.21	76.99 ± 0.04	70.28 ± 0.14	74.89 ± 0.06	76.93 ± 0.13
cGAN-KD + FitNet	70.43 ± 0.14	75.02 ± 0.29	69.72 ± 0.38	74.66 ± 0.37	77.52 ± 0.25	77.55 ± 0.17	70.70 ± 0.23	75.15 ± 0.29	77.15 ± 0.28
cGAN-KD + VID	70.05 ± 0.24	74.73 ± 0.21	69.56 ± 0.14	74.68 ± 0.19	77.00 ± 0.14	77.26 ± 0.13	70.75 ± 0.32	75.32 ± 0.30	77.13 ± 0.07
cGAN-KD + RKD	70.59 ± 0.29	74.65 ± 0.13	70.00 ± 0.12	74.23 ± 0.21	76.30 ± 0.12	77.25 ± 0.21	70.73 ± 0.24	75.03 ± 0.15	77.02 ± 0.32
cGAN-KD + CRD	71.29 ± 0.17	75.34 ± 0.23	<u>70.50 ± 0.21</u>	75.31 ± 0.03	77.27 ± 0.16	77.61 ± 0.27	71.38 ± 0.10	75.20 ± 0.23	77.50 ± 0.15
cGAN-KD + SSKD	72.00 ± 0.16	<u>75.60 ± 0.21</u>	71.63 ± 1.35	76.58 ± 0.27	78.67 ± 0.10	78.99 ± 0.07	72.96 ± 0.18	76.12 ± 0.25	77.99 ± 0.19

Teacher	DenseNet121 (79.98)	DenseNet121 (79.98)	DenseNet121 (79.98)	DenseNet121 (79.98)	DenseNet121 (79.98)	DenseNet121 (79.98)
Student	MobileNetV2	ResNet20	VGG8	ResNet8x4	ShuffleNetV1	ShuffleNetV2
NOKD	64.59 ± 0.34	69.22 ± 0.39	70.61 ± 0.44	72.74 ± 0.07	71.47 ± 0.28	72.63 ± 0.49
BLKD (2015)	68.21 ± 0.39	69.93 ± 0.25	<u>73.45 ± 0.31</u>	<u>74.32 ± 0.42</u>	<u>75.59 ± 0.15</u>	<u>76.44 ± 0.14</u>
TAKD (2020)	68.29 ± 0.04	69.89 ± 0.23	73.41 ± 0.16	74.10 ± 0.29	75.33 ± 0.42	75.98 ± 0.37
cGAN-KD	<u>68.35 ± 0.22</u>	<u>70.71 ± 0.10</u>	72.08 ± 0.21	72.90 ± 0.11	74.60 ± 0.48	75.22 ± 0.43
cGAN-KD + BLKD	70.86 ± 0.36	71.68 ± 0.39	75.24 ± 0.08	74.81 ± 0.25	77.44 ± 0.10	78.29 ± 0.20

Table 4: **ImageNet-100: Top-1 test accuracy (%) of compared KD methods. Bold and underline denote the best and the second best results, respectively.**

Teacher	ResNet110 (75.31)	WRN40×2 (77.67)	ResNet34 (81.54)	VGG19 (83.41)	VGG19 (83.41)
Student	ResNet20	WRN40×1	WRN40×1	VGG8	ShuffleNetV1
NOKD	65.25	69.98	69.98	77.36	75.02
BLKD (2015)	65.35	70.79	69.36	80.15	77.07
FitNet (2015)	66.20	71.46	71.38	80.26	NA
VID (2019)	66.76	71.38	71.34	81.03	77.41
RKD (2019)	66.45	71.37	69.81	80.70	77.46
CRD (2019)	66.79	72.13	70.39	81.17	77.65
SSKD (2020)	67.05	72.92	71.44	<u>81.85</u>	<u>78.93</u>
SemCKD (2021)	NA	71.46	71.79	80.74	77.72
SimKD (2022)	60.95	71.26	72.72	81.46	78.67
cGAN-KD	67.15	72.17	72.17	78.21	76.89
cGAN-KD + BLKD	66.87	72.83	72.18	80.29	78.41
cGAN-KD + FitNet	66.73	73.53	72.63	81.16	NA
cGAN-KD + VID	67.24	72.87	72.53	81.19	78.65
cGAN-KD + RKD	67.66	73.10	72.21	80.93	78.70
cGAN-KD + CRD	<u>67.91</u>	<u>73.18</u>	<u>73.06</u>	81.46	78.40
cGAN-KD + SSKD	68.58	74.15	73.31	82.46	80.30

For cGAN-KD-based methods, we adopt the SAGAN architecture (Zhang et al., 2019) and train one CcGAN model (SVDL+ILI) with DiffAugment for each dataset. We let $\rho = 0.7$ on both datasets. We generate 50,000 and 60,000 processed fake samples for the Steering Angle and UTKFace experiments, respectively.

All results of the regression experiments are reported in a **single trial**. Other implementation details such as learning rate, batch size, weight decay, number of epochs, seed, and optimizer are shown in Sections S.7 and S.8 in Appendix.

5.2.4. Experimental results

The quantitative results of both experiments are shown in Table 5. For Steering Angle, cGAN-KD outperforms NOKD with a large margin. Notably, the test error of WRN16×1 is reduced by $(5.74 - 1.79)/5.74 \times 100\% = 68.82\%$ on Steering Angle. FitNet and RKD perform surprisingly well on Steering Angle, and they outperform cGAN-KD under two teacher-student pairs (ResNet34-ShuffleNetV2 and VGG19-ShuffleNetV1). Thus, we also incorporate FitNet into cGAN-KD, i.e., cGAN-KD + FitNet. It beats all three existing KD methods in all teacher-student pairs. For UTKFace, cGAN-KD beats all existing KD methods with a large margin. For example, MobileNetV2’s test error is reduced by $(7.16 - 4.84)/7.16 \times 100\% = 32.40\%$ by using cGAN-KD, but the three feature-based KD methods do not have significant effects on this dataset. cGAN-KD + FitNet is substantially better than FitNet but slightly worse than cGAN-KD, implying we should not combine cGAN-KD with a less effective KD method. Please also note that, unlike many existing KD methods, cGAN-KD even outperforms the teacher models in the UTKFace experiment, implying CcGAN may generate new information helpful for the regression task.

Table 5: **The test mean absolute errors (MAE) of compared KD methods on Steering Angle and UTKFace.** The units of the test MAE for Steering Angle and UTKFace are degrees and years, respectively. Bold and underline denote the best and the second best results, respectively.

Steering Angle							
Teacher	ResNet34 (1.30)	ResNet34 (1.30)	ResNet34 (1.30)	ResNet34 (1.30)	VGG19 (1.10)	VGG19 (1.10)	VGG19 (1.10)
Student	ResNet20	ShuffleNetV2	WRN16×1	ResNet8x4	WRN40×1	ShuffleNetV1	ResNet56
NOKD	4.86	5.14	5.74	3.90	3.70	3.47	2.63
FitNet (2015)	2.18	2.23	2.16	2.69	2.15	2.14	1.93
AT (2017)	2.75	2.04	2.81	2.32	2.19	2.32	2.34
RKD (2019)	2.80	2.43	4.49	2.69	2.25	2.12	2.44
cGAN-KD	<u>1.54</u>	2.51	1.79	<u>2.15</u>	<u>1.52</u>	2.21	<u>1.55</u>
cGAN-KD + FitNet	1.53	1.68	<u>1.87</u>	1.82	1.40	2.05	1.46
UTKFace							
Teacher	ResNet34 (5.29)	ResNet34 (5.29)	ResNet34 (5.29)	ResNet34 (5.29)	VGG11 (5.12)	VGG11 (5.12)	VGG11 (5.12)
Student	WRN16×1	MobileNetV2	ResNet56	ShuffleNetV1	ResNet20	WRN40×1	ResNet8x4
NOKD	7.25	7.16	7.06	7.03	6.87	6.70	6.68
FitNet (2015)	7.04	6.86	6.78	6.93	6.52	6.68	6.25
AT (2017)	7.20	6.97	7.30	7.23	6.88	6.85	6.64
RKD (2019)	6.71	7.13	6.80	7.33	6.38	6.39	5.97
cGAN-KD	5.01	4.84	4.90	4.95	4.92	4.92	4.76
cGAN-KD + FitNet	<u>5.63</u>	<u>5.65</u>	<u>5.52</u>	<u>5.58</u>	<u>5.23</u>	<u>5.24</u>	<u>4.96</u>

5.3. Ablation study: the effect of different (sub-)modules of cGAN-KD

5.3.1. Some visual and quantitative illustration for M1 and M2

As illustrated in Section 3.3, the subsampling module (**M1**) can effectively improve the visual quality of fake images. In Fig. 5, we show some example fake images from the “indigo bunting” class in the ImageNet-100 experiment in Section 5.1. We can see fake images directly generated from a trained cGAN may contain many unrealistic images (marked by red rectangles in the second row). But the subsampling module (third row) can effectively drop most of them. Besides the subsampling module, as described in Section 3.4 and visualized in Fig. 5, the filtering sub-module can also enhance the visual quality. Some example fake images that are kept and dropped by filtering are shown in Figs. 6 and 7, where most remaining images are high-quality while most dropped images have poor visual quality.

M2 consists of two sequential sub-modules, i.e., filtering and replacement. In addition to improving visual quality, the primary function of filtering is to increase the label consistency of fake images. Two illustrative figures and a table are shown in Fig. 8 and Tab. 6, respectively. From them, we can conclude that the filtering sub-module can effectively rule out fake images whose assigned labels are far from their predicted

labels. Note that the predicted labels are assumed to be close to the actual labels of fake images, given that they are predictions from accurate teacher models. Fig. 8 and Tab. 6 also show that, on CIFAR-100 and ImageNet-100, the remaining images’ predicted labels are already consistent with their assigned labels after filtering, so the replacement sub-module is unnecessary for classification tasks.

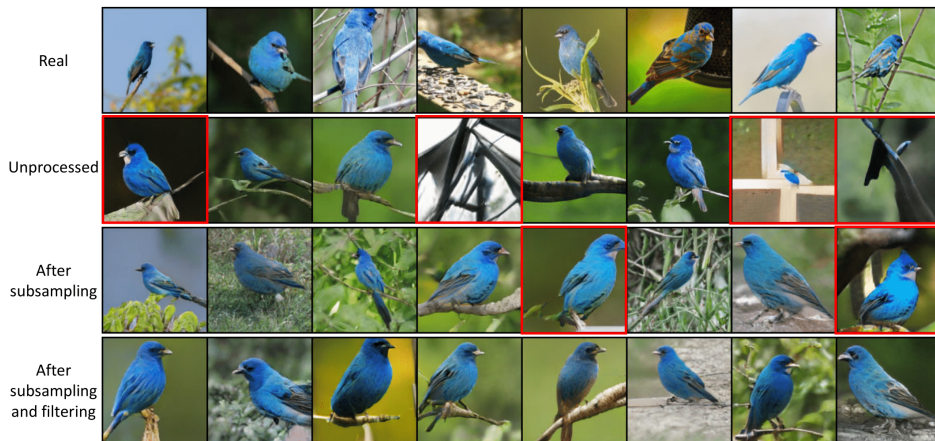


Fig. 5: **The subsampling and filtering (sub-)modules can effectively improve fake images’ visual quality.** Some example images are shown here for the “indigo bunting” class at 128×128 resolution in the ImageNet-100 experiment. The first and second rows includes ten real images and ten unprocessed fake images, respectively. The third and fourth rows include fake images processed by subsampling only and subsampling+filtering, respectively. We observe many unrealistic unprocessed fake images in the second row (marked in red rectangles). The subsampling module (third row) can effectively remove most of them and the filtering sub-module (fourth row) can further improve the visual quality.

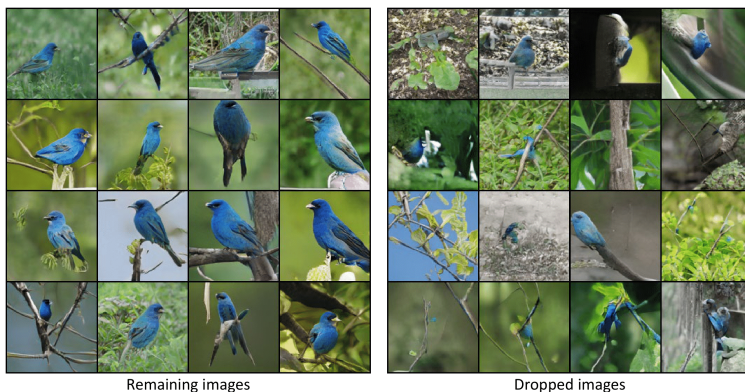


Fig. 6: **Some example fake images processed by the filtering sub-module for the “indigo bunting” class at 128×128 resolution in the ImageNet-100 experiment (classification) in Section 5.** The left image grid shows some fake images are not dropped by the filtering sub-module, while the right grid includes fake images that are dropped. Both Figs. 5 and 6 show that, as a side effect, the filtering sub-module can effectively drop most unrealistic fake images, so the overall visual quality is improved.

5.3.2. Effects of different (sub-)modules on the prediction precision

In this section, an ablation study is also designed to test the effectiveness of the subsampling, filtering, and replacement (for regression only) (sub-)modules in the cGAN-KD framework on CIFAR-100 and Steering Angle, aiming to show how cGAN-KD performs if these (sub-)modules are added into the framework one by one. In this study, other setups (e.g., M^g , ρ , and the teacher model) remain unchanged, and the results are reported based on a single trial. The quantitative result is visualized in Fig. 9. We can see that the precision



Fig. 7: **Some example fake images processed by the filtering sub-module at 64×64 resolution in the Steering Angle experiment (regression).** The left image grid shows some fake images are not dropped by the filtering sub-module, while the right grid includes fake images that are dropped. The right grid shows that, as a side effect, the filtering sub-module can effectively drop many unrealistic fake images (marked in red rectangles). Some realistic images are also dropped in the right image grid because they are not consistent with their assigned labels.

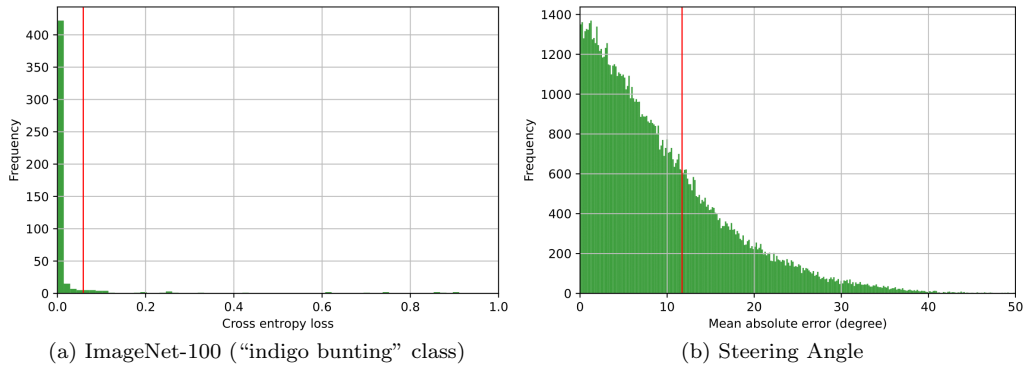


Fig. 8: **The histograms of cross entropy losses and mean absolute errors in the ImageNet-100 (classification) and Steering Angle (regression) experiments.** The red vertical lines represent the filtering threshold α (with $\rho = 0.9$ for ImageNet-100 and $\rho = 0.7$ for Steering Angle). The fake samples with errors larger than the threshold are dropped. In Fig. 8(a), we filter 500 fake images generated via **M1** for the “indigo bunting” class. Fig. 8(a) shows that, after the filtering, almost all remaining fake samples are label consistent, implying that it is unnecessary to apply replacement in classification. For the Steering Angle experiment, we filter 100,000 fake images generated by **M1** with a global α . Fig. 8(b) shows that the tail distribution of errors in regression is much heavier than that in classification. Thus, we propose a smaller ρ in regression, i.e., $\rho = 0.7$. Although the filtering sub-module can effectively remove fake samples with very large errors, the errors of most remaining fake samples are still non-zero. Therefore, we need the replacement sub-module to further adjust their labels.

Table 6: **The label consistency of fake images before or after filtering in the CIFAR-100 and ImageNet-100 experiments.** We first generate 50,000 fake images (500 images per class) from **M1** in each experiment. These fake images are then filtered by a pre-trained teacher model (DenseNet121 for CIFAR-100 and DenseNet161 for ImageNet-100) with $\rho = 0.9$. After filtering, there are 45,000 fake images left (450 images per class). Here, label consistency is the percentage of fake images whose assigned labels and predicted labels are equal. After filtering, almost all remaining images’ predicted labels are consistent with their assigned labels. Therefore, the replacement sub-module is not necessary for classification tasks.

CIFAR-100		ImageNet-100	
Before	After	Before	After
91.352%	97.802%	93.854%	99.064%

of student models gradually improves as we add these modules into cGAN-KD sequentially. The combination of these (sub-)modules leads to the highest precision.

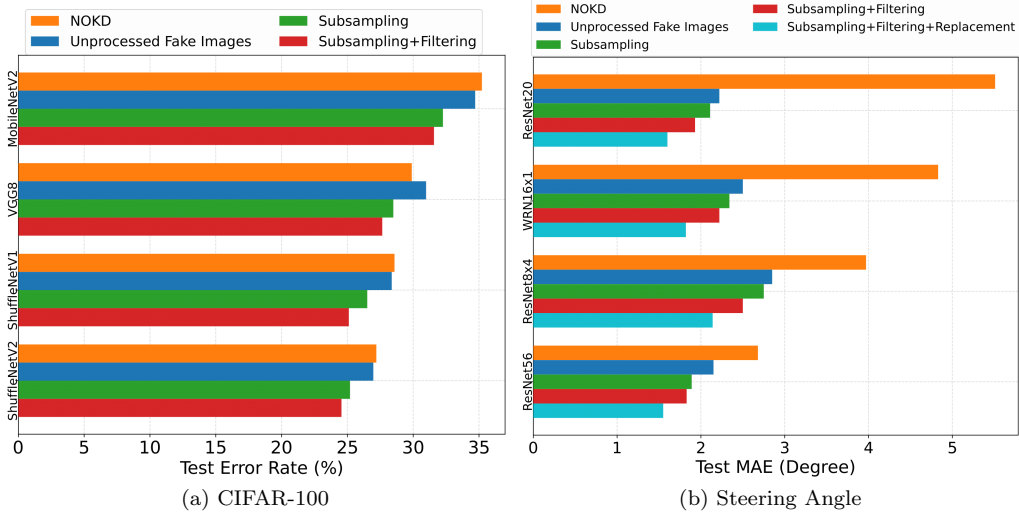


Fig. 9: **Ablation study: The effect of different (sub-)modules of cGAN-KD (subsampling, filtering, and replacement).** The precision of student models gradually improves as we add these (sub-)modules into cGAN-KD sequentially, implying the combination of these modules leads to the highest precision. Please note that unprocessed fake samples may cause adverse effects if directly used in data augmentation, e.g., VGG8 in the CIFAR-100 experiment.

5.4. Additional analysis

From Sections 5.4.1 to 5.4.3, we conduct some additional analyses to research the effects of M^g , ρ , and the selection of teacher in the cGAN-KD framework. Note that all results are reported in terms of a single trial due to time and facility constraints. We also provide a running time and memory cost comparison at the end of this section.

5.4.1. Sensitivity analysis on the fake sample size M^g

We conduct a sensitivity analysis on CIFAR-100 and Steering Angle to analyze the effect of different M^g . Compared with the main studies in Sections 5.1 and 5.2, we only vary M^g but keep other setups unchanged. The results of both datasets are shown in Figure 10. We can conclude that more processed fake images stabilize the student models' performance without significantly decreasing the precision, which confirms the necessity of a large M^g .

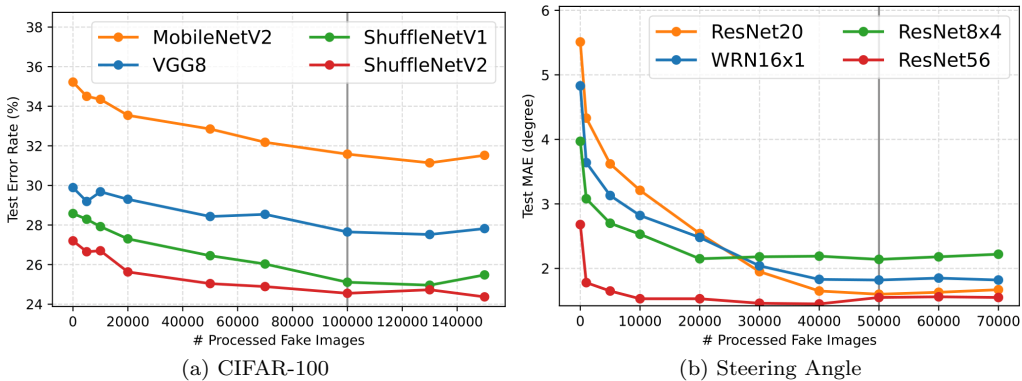


Fig. 10: **The effect of fake sample size M^g .** Gray lines indicate the M^g we use in our experiments.

5.4.2. Sensitivity analysis on the filtering quantile ρ

The effect of ρ , another important hyper-parameter, is also analyzed in this section on CIFAR-100 and Steering Angle. Compared with the main studies in Sections 5.1 and 5.2, we only vary ρ but keep other setups unchanged, and visualize the results in Fig. 11. From Fig. 11(a), we can see that the performance of student models fluctuates in a small range when $\rho \in [0.2, 0.98]$, and any ρ that is not extremely small or large (i.e., close to 0 or 1) often leads to good performance on CIFAR-100. Similarly, from Fig. 11(b), we can see that a $\rho \in [0.3, 0.8]$ often a good choice on the Steering Angle dataset. Fig. 11 implies that the recommended ρ in Section 3.4 (0.9 for classification and 0.7 for regression) often leads to desirable KD performance, and we generally don't need to carefully tune ρ in practice.

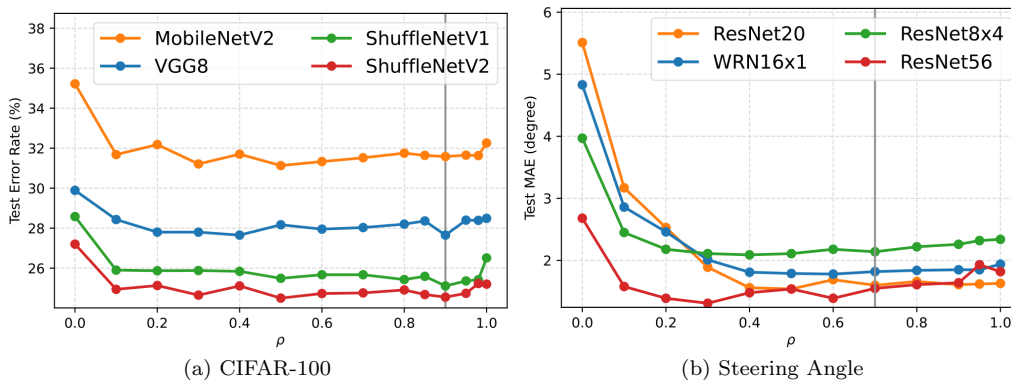


Fig. 11: **The effect of the filtering quantile ρ .** Gray lines indicate the ρ we use in our experiments. $\rho = 0$ corresponds to NOKD and $\rho = 1$ implies no filtering.

5.4.3. Sensitivity analysis on the teacher model's precision

We also test the effect of the teacher model's precision. This study chooses neural networks with different precision as the teacher model in the cGAN-KD framework. Table 7 shows that teachers with the highest accuracies often lead to the best KD results. Therefore, when implementing cGAN-KD, we should choose a teacher model with a precision as high as possible.

Table 7: **Sensitivity analysis of the effect of different teacher models in M2 on CIFAR-100 and Steering Angle.** We show below the Top-1 test accuracy (%) and test MAE (degree) of students under different teachers on CIFAR-100 and Steering Angle, respectively. The precision of different teachers on the test sets are shown in the parentheses.

CIFAR-100				
Teachers	NOKD	WRN40 \times 2 (75.82)	ResNet18 (77.98)	DenseNet121 (79.98)
Students				
MobileNetV2	64.78	68.24	68.33	68.42
VGG8	70.11	71.63	72.29	72.35
ShuffleNetV1	71.42	73.83	74.43	74.89
ShuffleNetV2	72.80	74.63	74.94	75.45
Steering Angle				
Teachers	NOKD	VGG8 (2.07)	ResNet18 (1.71)	VGG19 (1.06)
Students				
ResNet20	5.51	1.71	1.65	1.60
WRN16 \times 1	4.83	1.94	1.92	1.82
ResNet8 \times 4	3.97	2.27	2.22	2.14
ResNet56	2.68	1.65	1.55	1.55

5.4.4. Processing time and memory cost comparison

We also estimate the overall processing time and GPU memory required to implement cGAN-KD and some representative KD baselines on CIFAR-100, Steering Angle, and UTKFace in Figure 12, based on a single Tesla A100 GPU. Due to the implementation of cGANs, cDR-RS, and data augmentation, cGAN-KD-based

methods need more processing time and GPU memory than other KD methods; however, cGAN-KD-based methods often lead to better KD performance.

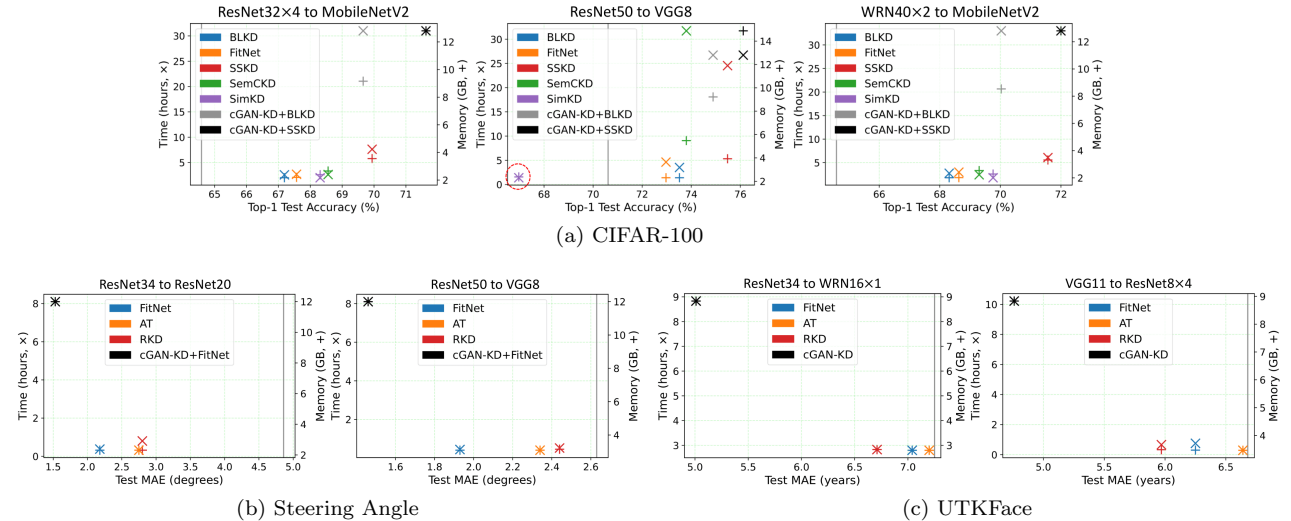


Fig. 12: **Processing time (marked by “x”) and memory cost (marked by “+”) comparison.** Gray lines represent the performance of NOKD.

6. Conclusion

As the first attempt, this paper proposes a unified knowledge distillation framework widely applicable for both classification and regression (with a scalar response) tasks. Fundamentally different from many existing knowledge distillation methods, we propose distilling and transferring knowledge from the teacher model to the student model through cGAN-generated samples, termed cGAN-KD. First, cGAN models are trained to generate a sufficient number of fake image samples. Then, high quality samples are obtained via subsampling and filtering procedures. Essentially, the knowledge is distilled by adjusting fake image labels utilizing the teacher model. Finally, the distilled knowledge is transferred to student models by training them on these knowledge-conveyed samples. The proposed framework is architecture-agnostic and it is compatible with existing state-of-the-art knowledge distillation models. We also derive the error bound of a student model trained in the cGAN framework for theoretical guidance. Extensive experiments demonstrate that the cGAN-KD incorporated methods can achieve state-of-the-art knowledge distillation performances for both classification and regression tasks.

Acknowledgments

This work was supported by the Natural Sciences and Engineering Research Council of Canada (NSERC) under Grants CRDPJ 476594-14, RGPIN-2019-05019, and RGPAS2017-507965.

References

- Ahn, S., Hu, S. X., Damianou, A., Lawrence, N. D., & Dai, Z. (2019). Variational information distillation for knowledge transfer. In *Proceedings of the IEEE/CVF Conference on Computer Vision and Pattern Recognition* (pp. 9163–9171).
- Ali-Gombe, A., & Elyan, E. (2019). MFC-GAN: Class-imbalanced dataset classification using multiple fake class generative adversarial network. *Neurocomputing*, 361, 212–221.
- Arazo, E., Ortego, D., Albert, P., O’Connor, N. E., & McGuinness, K. (2020). Pseudo-labeling and confirmation bias in deep semi-supervised learning. In *2020 International Joint Conference on Neural Networks (IJCNN)* (pp. 1–8).

- Brock, A., Donahue, J., & Simonyan, K. (2019). Large scale GAN training for high fidelity natural image synthesis. In *International Conference on Learning Representations*.
- Buciluă, C., Caruana, R., & Niculescu-Mizil, A. (2006). Model compression. In *Proceedings of the 12th ACM SIGKDD International Conference on Knowledge Discovery and Data Mining* (pp. 535–541).
- Cao, Z., Long, M., Wang, J., & Yu, P. S. (2017). Hashnet: Deep learning to hash by continuation. In *Proceedings of the IEEE International Conference on Computer Vision* (pp. 5608–5617).
- Chen, D., Mei, J.-P., Zhang, H., Wang, C., Feng, Y., & Chen, C. (2022). Knowledge distillation with the reused teacher classifier. In *Proceedings of the IEEE/CVF Conference on Computer Vision and Pattern Recognition* (pp. 11933–11942).
- Chen, D., Mei, J.-P., Zhang, Y., Wang, C., Wang, Z., Feng, Y., & Chen, C. (2021a). Cross-layer distillation with semantic calibration. In *Proceedings of the AAAI Conference on Artificial Intelligence* (pp. 7028–7036). volume 35.
- Chen, H., Wang, Y., Xu, C., Yang, Z., Liu, C., Shi, B., Xu, C., Xu, C., & Tian, Q. (2019). Data-free learning of student networks. In *Proceedings of the IEEE/CVF International Conference on Computer Vision* (pp. 3514–3522).
- Chen, P., Liu, S., Zhao, H., & Jia, J. (2021b). Distilling knowledge via knowledge review. In *Proceedings of the IEEE/CVF Conference on Computer Vision and Pattern Recognition* (pp. 5008–5017).
- Chen, S. (2018a). How a high school junior made a self-driving car? @ONLINE. <https://towardsdatascience.com/how-a-high-school-junior-made-a-self-driving-car-705fa9b6e860>.
- Chen, S. (2018b). The Steering Angle dataset @ONLINE. <https://github.com/SullyChen/driving-datasets>.
- Chen, T., Kornblith, S., Norouzi, M., & Hinton, G. (2020). A simple framework for contrastive learning of visual representations. In *International Conference on Machine Learning* (pp. 1597–1607).
- Deng, J., Dong, W., Socher, R., Li, L.-J., Li, K., & Fei-Fei, L. (2009). ImageNet: A large-scale hierarchical image database. In *Proceedings of the IEEE Conference on Computer Vision and Pattern Recognition* (pp. 248–255).
- DeVries, T., Romero, A., Pineda, L., Taylor, G. W., & Drozdal, M. (2019). On the evaluation of conditional GANs. *arXiv preprint arXiv:1907.08175*, .
- Ding, X., Wang, Y., Wang, Z. J., & Welch, W. J. (2022). Efficient subsampling of realistic images from GANs conditional on a class or a continuous variable. *arXiv preprint arXiv:2103.11166*, .
- Ding, X., Wang, Y., Xu, Z., Welch, W. J., & Wang, Z. J. (2021a). CcGAN: Continuous conditional generative adversarial networks for image generation. In *International Conference on Learning Representations*.
- Ding, X., Wang, Y., Xu, Z., Welch, W. J., & Wang, Z. J. (2021b). Continuous conditional generative adversarial networks: Novel empirical losses and label input mechanisms. *arXiv preprint arXiv:2011.07466*, .
- Ding, X., Wang, Z. J., & Welch, W. J. (2020). Subsampling generative adversarial networks: Density ratio estimation in feature space with softplus loss. *IEEE Transactions on Signal Processing*, 68, 1910–1922.
- Frid-Adar, M., Klang, E., Amitai, M., Goldberger, J., & Greenspan, H. (2018). Synthetic data augmentation using GAN for improved liver lesion classification. In *2018 IEEE 15th International Symposium on Biomedical Imaging* (pp. 289–293).
- Fukushima, K. (1969). Visual feature extraction by a multilayered network of analog threshold elements. *IEEE Transactions on Systems Science and Cybernetics*, 5, 322–333.
- Fukushima, K., & Miyake, S. (1982). Neocognitron: A self-organizing neural network model for a mechanism of visual pattern recognition. In *Competition and Cooperation in Neural Nets* (pp. 267–285).
- Gibbs, A. L., & Su, F. E. (2002). On choosing and bounding probability metrics. *International Statistical Review*, 70, 419–435.
- Goodfellow, I., Pouget-Abadie, J., Mirza, M., Xu, B., Warde-Farley, D., Ozair, S., Courville, A., & Bengio, Y. (2014). Generative adversarial nets. In *Advances in Neural Information Processing Systems 27* (pp. 2672–2680).
- Gou, J., Yu, B., Maybank, S. J., & Tao, D. (2021). Knowledge distillation: A survey. *International Journal of Computer Vision*, 129, 1789–1819.
- Heo, B., Lee, M., Yun, S., & Choi, J. Y. (2019). Knowledge transfer via distillation of activation boundaries formed by hidden neurons. In *Proceedings of the AAAI Conference on Artificial Intelligence* (pp. 3779–3787). volume 33.
- Heusel, M., Ramsauer, H., Unterthiner, T., Nessler, B., & Hochreiter, S. (2017). GANs trained by a two time-scale update rule converge to a local nash equilibrium. In *Advances in Neural Information Processing Systems* (pp. 6626–6637).
- Hinton, G., Vinyals, O., & Dean, J. (2015). Distilling the knowledge in a neural network. *NIPS Deep Learning Workshop*, .
- Huang, G., Liu, Z., Van Der Maaten, L., & Weinberger, K. Q. (2017). Densely connected convolutional networks. In *Proceedings of the IEEE Conference on Computer Vision and Pattern Recognition* (pp. 4700–4708).
- Karras, T., Aittala, M., Hellsten, J., Laine, S., Lehtinen, J., & Aila, T. (2020a). Training generative adversarial networks with limited data. *Advances in Neural Information Processing Systems*, 33, 12104–12114.
- Karras, T., Laine, S., & Aila, T. (2019). A style-based generator architecture for generative adversarial networks. In *Proceedings of the IEEE Conference on Computer Vision and Pattern Recognition* (pp. 4401–4410).
- Karras, T., Laine, S., Aittala, M., Hellsten, J., Lehtinen, J., & Aila, T. (2020b). Analyzing and improving the image quality of StyleGAN. In *Proceedings of the IEEE/CVF Conference on Computer Vision and Pattern Recognition* (pp. 8110–8119).
- Kim, J., Park, S., & Kwak, N. (2018). Paraphrasing complex network: Network compression via factor transfer. *Advances in Neural Information Processing Systems*, 31.
- Krizhevsky, A., Hinton, G. et al. (2009). *Learning multiple layers of features from tiny images*. Technical Report Citeseer.
- Lafferty, J., Liu, H., & Wasserman, L. (2010). Concentration of measure. URL: <http://www.stat.cmu.edu/~larry/=sml/Concentration.pdf>.
- Lee, D.-H. et al. (2013). Pseudo-label: The simple and efficient semi-supervised learning method for deep neural networks. In *Workshop on Challenges in Representation Learning, ICML*. volume 3.
- Li, Y., Wang, Q., Zhang, J., Hu, L., & Ouyang, W. (2021). The theoretical research of generative adversarial networks: an overview. *Neurocomputing*, 435, 26–41.
- Liu, P., Liu, W., Ma, H., Jiang, Z., & Seok, M. (2020). KTAN: Knowledge transfer adversarial network. In *2020 International*

- Joint Conference on Neural Networks (IJCNN)* (pp. 1–7).
- Lopes, R. G., Fenu, S., & Starner, T. (2017). Data-free knowledge distillation for deep neural networks. *arXiv preprint arXiv:1710.07535*, .
- Mariani, G., Scheidegger, F., Istrate, R., Bekas, C., & Malossi, C. (2018). BAGAN: Data augmentation with balancing GAN. *arXiv preprint arXiv:1803.09655*, .
- Mirza, M., & Osindero, S. (2014). Conditional generative adversarial nets. *arXiv preprint arXiv:1411.1784*, .
- Mirzadeh, S. I., Farajtabar, M., Li, A., Levine, N., Matsukawa, A., & Ghasemzadeh, H. (2020). Improved knowledge distillation via teacher assistant. In *Proceedings of the AAAI Conference on Artificial Intelligence* (pp. 5191–5198). volume 34.
- Miyato, T., Kataoka, T., Koyama, M., & Yoshida, Y. (2018). Spectral normalization for generative adversarial networks. In *International Conference on Learning Representations*.
- Miyato, T., & Koyama, M. (2018). cGANs with projection discriminator. In *International Conference on Learning Representations*.
- Mohri, M., Rostamizadeh, A., & Talwalkar, A. (2018). *Foundations of machine learning*. MIT Press.
- Odena, A., Olah, C., & Shlens, J. (2017). Conditional image synthesis with auxiliary classifier gans. In *International Conference on Machine Learning* (pp. 2642–2651).
- Park, W., Kim, D., Lu, Y., & Cho, M. (2019). Relational knowledge distillation. In *Proceedings of the IEEE/CVF Conference on Computer Vision and Pattern Recognition* (pp. 3967–3976).
- Passalis, N., & Tefas, A. (2018). Learning deep representations with probabilistic knowledge transfer. In *Proceedings of the European Conference on Computer Vision (ECCV)* (pp. 268–284).
- Romero, A., Ballas, N., Kahou, S. E., Chassang, A., Gatta, C., & Bengio, Y. (2015). FitNet: Hints for thin deep nets. In *International Conference on Learning Representations*.
- Ruffy, F., & Chahal, K. (2019). The state of knowledge distillation for classification. *arXiv preprint arXiv:1912.10850*, .
- Saputra, M. R. U., De Gusmao, P. P., Almalioglu, Y., Markham, A., & Trigoni, N. (2019). Distilling knowledge from a deep pose regressor network. In *Proceedings of the IEEE/CVF International Conference on Computer Vision* (pp. 263–272).
- Shen, Z., He, Z., & Xue, X. (2019). Meal: Multi-model ensemble via adversarial learning. In *Proceedings of the AAAI Conference on Artificial Intelligence* (pp. 4886–4893). volume 33.
- Simonyan, K., & Zisserman, A. (2014). Very deep convolutional networks for large-scale image recognition. *arXiv preprint arXiv:1409.1556*, .
- Sixt, L., Wild, B., & Landgraf, T. (2018). RenderGAN: Generating realistic labeled data. *Frontiers in Robotics and AI*, 5, 66.
- Tian, Y., Krishnan, D., & Isola, P. (2019). Contrastive representation distillation. In *International Conference on Learning Representations*.
- Tran, N.-T., Tran, V.-H., Nguyen, N.-B., Nguyen, T.-K., & Cheung, N.-M. (2021). On data augmentation for GAN training. *IEEE Transactions on Image Processing*, 30, 1882–1897.
- Tung, F., & Mori, G. (2019). Similarity-preserving knowledge distillation. In *Proceedings of the IEEE/CVF International Conference on Computer Vision* (pp. 1365–1374).
- Wang, C., Chen, D., Mei, J.-P., Zhang, Y., Feng, Y., & Chen, C. (2022). SemCKD: Semantic calibration for cross-layer knowledge distillation. *IEEE Transactions on Knowledge and Data Engineering*, .
- Wang, L., & Yoon, K.-J. (2021). Knowledge distillation and student-teacher learning for visual intelligence: A review and new outlooks. *IEEE Transactions on Pattern Analysis and Machine Intelligence*, .
- Wang, X., Zhang, R., Sun, Y., & Qi, J. (2018). KDGAN: Knowledge distillation with generative adversarial networks. *Advances in Neural Information Processing Systems*, 31.
- Wu, E., Wu, K., Cox, D., & Lotter, W. (2018). Conditional infilling GANs for data augmentation in mammogram classification. In *Image Analysis for Moving Organ, Breast, and Thoracic Images* (pp. 98–106).
- Xu, G., Liu, Z., Li, X., & Loy, C. C. (2020). Knowledge distillation meets self-supervision. In *European Conference on Computer Vision* (pp. 588–604).
- Xu, X., Li, Y., & Yuan, C. (2021). Conditional image generation with one-vs-all classifier. *Neurocomputing*, 434, 261–267.
- Xu, Z., Hsu, Y.-C., & Huang, J. (2018). Training shallow and thin networks for acceleration via knowledge distillation with conditional adversarial networks. *ICLR 2018 Workshop*, .
- Yin, H., Molchanov, P., Alvarez, J. M., Li, Z., Mallya, A., Hoiem, D., Jha, N. K., & Kautz, J. (2020). Dreaming to distill: Data-free knowledge transfer via deepinversion. In *Proceedings of the IEEE/CVF Conference on Computer Vision and Pattern Recognition* (pp. 8715–8724).
- Zagoruyko, S., & Komodakis, N. (2017). Paying more attention to attention: Improving the performance of convolutional neural networks via attention transfer. In *International Conference on Learning Representations*.
- Zhang, H., Goodfellow, I., Metaxas, D., & Odena, A. (2019). Self-attention generative adversarial networks. In *International Conference on Machine Learning* (pp. 7354–7363).
- Zhang, Z., Song, Y., & Qi, H. (2017). Age progression/regression by conditional adversarial autoencoder. In *Proceedings of the IEEE Conference on Computer Vision and Pattern Recognition* (pp. 5810–5818).
- Zhao, Q., Dong, J., Yu, H., & Chen, S. (2020a). Distilling ordinal relation and dark knowledge for facial age estimation. *IEEE Transactions on Neural Networks and Learning Systems*, 32, 3108–3121.
- Zhao, S., Liu, Z., Lin, J., Zhu, J.-Y., & Han, S. (2020b). Differentiable augmentation for data-efficient GAN training. *Advances in Neural Information Processing Systems*, 33.
- Zhao, Z., Zhang, Z., Chen, T., Singh, S., & Zhang, H. (2020c). Image augmentations for GAN training. [arXiv:2006.02595](https://arxiv.org/abs/2006.02595).
- Zhou, R., Jiang, C., & Xu, Q. (2021). A survey on generative adversarial network-based text-to-image synthesis. *Neurocomputing*, 451, 316–336.
- Zhu, X., Liu, Y., Li, J., Wan, T., & Qin, Z. (2018). Emotion classification with data augmentation using generative adversarial

networks. In *Pacific-Asia Conference on Knowledge Discovery and Data Mining* (pp. 349–360).

Supplementary Material

S.1. GitHub repository

Please find some example codes for this paper at

https://github.com/UBCDingXin/cGAN-based_KD

S.2. Resources for implementing cGANs, Subsampling and KD Methods

To implement TAKD, we refer to

<https://github.com/imirzadeh/Teacher-Assistant-Knowledge-Distillation>

To implement SSKD, we refer to

<https://github.com/xuguodong03/SSKD>

To implement ReviewKD, we refer to

<https://github.com/dvlab-research/ReviewKD>

To implement SemCKD, we refer to

<https://github.com/DefangChen/SemCKD>

To implement SimKD, we refer to

<https://github.com/DefangChen/SimKD>

To implement other KD methods in our experiments, we refer to

<https://github.com/HobbitLong/RepDistiller>

To implement BigGAN, we refer to

<https://github.com/ajbrock/BigGAN-PyTorch>

To implement CcGAN, we refer to

https://github.com/UBCDingXin/improved_CcGAN

To implement DiffAugment, we refer to

<https://github.com/mit-han-lab/data-efficient-gans>

To implement cDR-RS, we refer to

<https://github.com/UBCDingXin/cDR-RS>

S.3. Proof of Theorem 1

Proof. We first decompose $\mathcal{V}(\hat{f}_s) - \mathcal{V}(f^*)$ as follows

$$\begin{aligned}
& \mathcal{V}(\hat{f}_s) - \mathcal{V}(f^*) \\
&= \mathcal{V}(\hat{f}_s) - \widehat{\mathcal{V}}(\hat{f}_s) + \widehat{\mathcal{V}}(\hat{f}_s) - \widehat{\mathcal{V}}(f_s^\circ) + \widehat{\mathcal{V}}(f_s^\circ) - \mathcal{V}(f_s^\circ) + \mathcal{V}(f_s^\circ) - \mathcal{V}(f^*) \\
&\quad (\text{by } \widehat{\mathcal{V}}(\hat{f}_s) - \widehat{\mathcal{V}}(f_s^\circ) \leq 0) \\
&\leq \mathcal{V}(\hat{f}_s) - \widehat{\mathcal{V}}(\hat{f}_s) + \widehat{\mathcal{V}}(f_s^\circ) - \mathcal{V}(f_s^\circ) + \mathcal{V}(f_s^\circ) - \mathcal{V}(f^*) \\
&\leq 2 \sup_{f_s \in \mathcal{F}_s} \left| \widehat{\mathcal{V}}(f_s) - \mathcal{V}(f_s) \right| + \mathcal{V}(f_s^\circ) - \mathcal{V}(f^*). \tag{S.1}
\end{aligned}$$

The second term $\mathcal{V}(f_s^\circ) - \mathcal{V}(f^*)$ in Eq. (S.1) is a non-negative number because the student model's hypothesis space \mathcal{F}_s may not cover the optimal predictor f^* . In Eq. (S.1), $\sup_{f_s \in \mathcal{F}_s} \left| \widehat{\mathcal{V}}(f_s) - \mathcal{V}(f_s) \right|$ can be bounded as follows. Using the triangular inequality and **A4** (i.e., boundedness of \mathcal{L}) yields

$$\begin{aligned}
& \sup_{f_s \in \mathcal{F}_s} \left| \widehat{\mathcal{V}}(f_s) - \mathcal{V}(f_s) \right| \\
&= \sup_{f_s \in \mathcal{F}_s} \left| \frac{1}{N^r + M^g} \sum_{(\mathbf{x}_i, y_i) \in D_{\text{aug}}} \mathcal{L}(f_s(\mathbf{x}_i), y_i) - \mathbb{E}_{(\mathbf{x}, y) \sim p_r(\mathbf{x}, y)} [\mathcal{L}(f_s(\mathbf{x}), y)] \right| \\
&\quad (\text{by the triangular inequality}) \\
&\leq \sup_{f_s \in \mathcal{F}_s} \left| \frac{1}{N^r + M^g} \sum_{(\mathbf{x}_i, y_i) \in D_{\text{aug}}} \mathcal{L}(f_s(\mathbf{x}_i), y_i) - \mathbb{E}_{(\mathbf{x}, y) \sim p_\theta(\mathbf{x}, y)} [\mathcal{L}(f_s(\mathbf{x}), y)] \right| \\
&\quad + \sup_{f_s \in \mathcal{F}_s} \left| \mathbb{E}_{(\mathbf{x}, y) \sim p_\theta(\mathbf{x}, y)} [\mathcal{L}(f_s(\mathbf{x}), y)] - \mathbb{E}_{(\mathbf{x}, y) \sim p_r(\mathbf{x}, y)} [\mathcal{L}(f_s(\mathbf{x}), y)] \right| \\
&\quad (\text{by the Boundedness assumption **A4**}) \\
&= C_{\mathcal{L}} \sup_{f_s \in \mathcal{F}_s} \left| \frac{1}{N^r + M^g} \sum_{(\mathbf{x}_i, y_i) \in D_{\text{aug}}} \frac{1}{C_{\mathcal{L}}} \mathcal{L}(f_s(\mathbf{x}_i), y_i) - \mathbb{E}_{(\mathbf{x}, y) \sim p_\theta(\mathbf{x}, y)} \left[\frac{1}{C_{\mathcal{L}}} \mathcal{L}(f_s(\mathbf{x}), y) \right] \right| \tag{S.2}
\end{aligned}$$

$$+ \sup_{f_s \in \mathcal{F}_s} \left| \mathbb{E}_{(\mathbf{x}, y) \sim p_\theta(\mathbf{x}, y)} [\mathcal{L}(f_s(\mathbf{x}), y)] - \mathbb{E}_{(\mathbf{x}, y) \sim p_r(\mathbf{x}, y)} [\mathcal{L}(f_s(\mathbf{x}), y)] \right|. \tag{S.3}$$

For Eq. (S.2), we apply the Rademacher bound (Lafferty et al., 2010, Thm 7.7.1), yielding that with at least probability $1 - \delta$,

$$\begin{aligned}
& C_{\mathcal{L}} \sup_{f_s \in \mathcal{F}_s} \left| \frac{1}{N^r + M^g} \sum_{(\mathbf{x}_i, y_i) \in D_{\text{aug}}} \frac{1}{C_{\mathcal{L}}} \mathcal{L}(f_s(\mathbf{x}_i), y_i) - \mathbb{E}_{(\mathbf{x}, y) \sim p_\theta(\mathbf{x}, y)} \left[\frac{1}{C_{\mathcal{L}}} \mathcal{L}(f_s(\mathbf{x}), y) \right] \right| \\
&\leq 2C_{\mathcal{L}} \widehat{\mathcal{R}}_{N^r + M^g}(\mathcal{F}_s) + C_{\mathcal{L}} \sqrt{\frac{4}{N^r + M^g} \log \left(\frac{2}{\delta} \right)}. \tag{S.4}
\end{aligned}$$

Before we bound Eq. (S.3), we first review the definition of the total variation distance (Gibbs & Su, 2002) between any two distributions P and Q , i.e.,

$$TV(P, Q) := \frac{1}{2} \sup_{|g| \leq 1} \left| \int g dP - \int g dQ \right|.$$

where g is a measurable function. Thus,

$$\begin{aligned}
& TV(p_r, \theta p_r + (1 - \theta)p_g^\rho) \\
&= \frac{1}{2} \sup_{|g| \leq 1} \left| \mathbb{E}_{(\mathbf{x}, y) \sim p_\theta(\mathbf{x}, y)} [g(\mathbf{x}, y)] - \mathbb{E}_{(\mathbf{x}, y) \sim p_r(\mathbf{x}, y)} [g(\mathbf{x}, y)] \right| \\
&= \frac{1}{2} \sup_{|g| \leq 1} \left\{ (1 - \theta) \cdot \left| \mathbb{E}_{(\mathbf{x}, y) \sim p_g^\rho(\mathbf{x}, y)} [g(\mathbf{x}, y)] - \mathbb{E}_{(\mathbf{x}, y) \sim p_r(\mathbf{x}, y)} [g(\mathbf{x}, y)] \right| \right\} \\
&= (1 - \theta) \cdot TV(p_r, p_g^\rho). \tag{S.5}
\end{aligned}$$

Since f_s is measurable (by **A2**) and \mathcal{L} is continuous, $\mathcal{L}(f_s(\mathbf{x}), y)$ is also measurable. Let $\mathcal{L}(f_s(\mathbf{x}), y)/C_{\mathcal{L}}$ be $g(\mathbf{x}, y)$ in Eq. (S.5), then by **A3** (i.e., the distribution gap between p_r and p_g^ρ), we have

$$\begin{aligned}
& \sup_{f_s \in \mathcal{F}_s} \left| \mathbb{E}_{(\mathbf{x}, y) \sim p_\theta(\mathbf{x}, y)} [\mathcal{L}(f_s(\mathbf{x}), y)] - \mathbb{E}_{(\mathbf{x}, y) \sim p_r(\mathbf{x}, y)} [\mathcal{L}(f_s(\mathbf{x}), y)] \right| \\
&= 2C_{\mathcal{L}}(1 - \theta) (C_{M1} + \Theta(\mathbb{E}_{(\mathbf{x}, y) \sim p_r(\mathbf{x}, y)} [\mathcal{L}(f_t(\mathbf{x}), y)]). \tag{S.6}
\end{aligned}$$

Combining Eqs. (S.4) and (S.6), we can get

$$\begin{aligned}
& \sup_{f_s \in \mathcal{F}_s} \left| \widehat{\mathcal{V}}(f_s) - \mathcal{V}(f_s) \right| \\
&\leq 2C_{\mathcal{L}} \widehat{\mathcal{R}}_{N^r + M^g}(\mathcal{F}_s) + C_{\mathcal{L}} \sqrt{\frac{4}{N^r + M^g} \log\left(\frac{2}{\delta}\right)} \\
&\quad + 2C_{\mathcal{L}}(1 - \theta) (C_{M1} + \Theta(\mathbb{E}_{(\mathbf{x}, y) \sim p_r(\mathbf{x}, y)} [\mathcal{L}(f_t(\mathbf{x}), y)]). \tag{S.7}
\end{aligned}$$

Finally, incorporating Eq. (S.7) into Eq. (S.1), we obtain the inequality (i.e., Eq. (7)) in Theorem 1, which completes the proof. \square

S.4. Evolution of fake data and their distributions after applying M1 and M2

S.5. More details of experiments on the CIFAR-100 dataset

We first train some popular neural networks from scratch on the training set of CIFAR-100. Following Xu et al. (2020), all these neural networks are trained for 240 epochs with the SGD optimizer, initial learning rate 0.05 (but 0.01 for ShuffleNet and MobileNetV2; decays at epoch 150, 180, and 210 with factor 0.1), weight decay 5×10^{-4} , and batch size 64. The number of parameters, inference speed, and Top-1/5 test accuracies of these neural networks are shown in Table S.5.8. MobileNetV2, ResNet20, VGG8, WRN40×1, ShuffleNetV1, ResNet8x4, ShuffleNetV2, and WRN16×2 are chosen as students due to their low Top-1 test accuracies. DenseNet121 is chosen as the teacher model f_t in cGAN-KD due to its highest Top-1 test accuracy. Some of these neural networks' checkpoints are used in the implementation of existing KD methods.

To implement BLKD and TAKD, we set $\lambda_{KD} = 0.5$ and $T = 5$ following Ruffey & Chahal (2019). In TAKD, the precision of a good TA model is usually the average of those of the teacher and student models (Mirzadeh et al., 2020). Based on this principle, the TA models for all teacher-student pairs are chosen and shown in Table S.5.9. To implement SSKD, we follow the default setups in Xu et al. (2020) and the corresponding GitHub repository. To implement ReviewKD, we follow the default setups in Chen et al. (2021b) and the corresponding GitHub repository. To implement SemCKD (Chen et al., 2021a; Wang et al., 2022) and SimKD (Chen et al., 2022), we use their official codes and default setups. We use the setups suggested by CRD (Tian et al., 2019) to implement other KD methods.

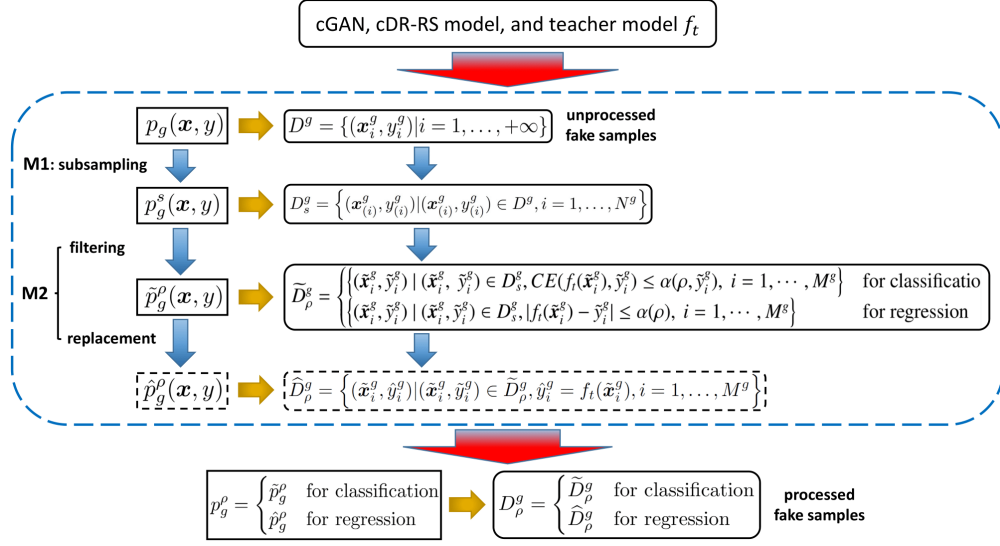


Fig. S.4.13: **Evolution of fake data and their distributions after applying M1 and M2.** Fake datasets are denoted by D with or without hat, tilde, superscripts or subscripts, e.g., D_s^g . The density functions of fake data’s distributions are denoted by $p(\mathbf{x}, y)$ with or without hat, tilde, superscripts or subscripts, e.g., $p_g^s(\mathbf{x}, y)$. The replacement sub-module is enabled only for regression problems. The number of samples after filtering is smaller than or equal to that after subsampling ($M^g \leq N^g$). The filtering threshold α is related to a hyper-parameter ρ or a class label. It is defined as the ρ -th quantile of errors between predicted and assigned labels of fake images. For classification, we have one α for one class, so that we conduct filtering within each class. For regression, we have a global α to filter all fake images. Please refer to Section 3.4 for the definition of α and the selection of ρ .

As for the implementation of cGAN-KD-based methods, we first train a BigGAN for 2,000 epochs with a batch size 512. DiffAugment (Zhao et al., 2020b) is enabled in the GAN training with the strongest transformation combination (Color + Translation + Cutout). Then, we implement cDR-RS to subsample fake images with the setups suggested by Ding et al. (2022). We choose DenseNet121 to filter fake images with $\rho = 0.9$. We generate 1000 processed fake images for each class (100,000 fake samples in total), which are then used to augment the training set.

cGAN-KD alone and cGAN-KD + X (excluding SSKD): We first initialize student models with their NOKD checkpoints. Then, we train students on the augmented dataset for 240 epochs with the SGD optimizer, initial learning rate 0.01 (decays at epoch 150, 180, and 210 with factor 0.1), weight decay 5×10^{-4} , and batch size 128.

cGAN-KD+SSKD: Initialize student models with their SSKD checkpoints. Then, we train students on the augmented dataset for 240 epochs with the SGD optimizer, initial learning rate 0.01 (decays at epoch 150, 180, and 210 with factor 0.1), weight decay 1×10^{-4} , and batch size 128.

We repeat all KD experiments four times and report the average results. The random seeds used in this experiment are shown in Table S.5.10. Please refer to our codes for more detailed experimental setup.

S.6. More details of experiments on the ImageNet-100 dataset

We first train some popular neural networks from scratch on the training set of ImageNet-100. Following Xu et al. (2020), all these neural networks are trained for 240 epochs with the SGD optimizer, initial learning rate 0.05 (but 0.01 for ShuffleNet and MobileNetV2; decays at epoch 150, 180, and 210 with factor 0.1), weight decay 5×10^{-4} , and batch size 128. The number of parameters, inference speed, and Top-1/5 test accuracies of these neural networks are shown in Table S.6.11. ResNet20, WRN40 \times 1, WRN16 \times 2, ResNet8 \times 4, ResNet56, MobileNetV2, ShuffleNetV1, and VGG8 are chosen as students due to their low Top-1 test accuracies. DenseNet161 is chosen as the teacher model f_t in cGAN-KD due to its highest Top-1 test accuracy. Some of these neural networks’ checkpoints are used in the implementation of existing KD methods.

Table S.5.8: Test accuracy, number of parameters, and inference speed of different neural networks on CIFAR-100. The inference speed is measured by processing 10,000 images with batch size 64 on a single RTX 2080TI. Since DenseNet121 has the highest Top-1 test accuracy, it is chosen as the teacher model f_t in cGAN-KD.

Models	# Params	Inference speed (images/second)	Test Accuracy \uparrow (Top-1)	Test Accuracy \uparrow (Top 5)
VGG8	3,965,028	5217	70.11	90.82
VGG11	9,277,284	5011	71.64	90.49
VGG13	9,462,180	4571	74.85	92.32
VGG19	20,086,692	3778	73.88	91.77
ResNet20	278,324	4542	68.83	91.10
ResNet56	861,620	3374	72.67	92.41
ResNet110	1,736,564	2322	73.27	92.71
ResNet8x4	1,233,540	4692	72.77	93.10
ResNet32x4	7,433,860	2340	79.11	94.64
ResNet18	11,220,132	2192	77.98	94.04
ResNet34	21,328,292	2384	78.94	94.65
ResNet50	23,705,252	1876	79.51	95.02
WRN16 \times 2	703,284	4821	73.02	92.94
WRN40 \times 1	569,780	3956	71.35	92.02
WRN40 \times 2	2,255,156	3895	75.82	93.53
DenseNet121	7,048,548	1421	79.98	95.04
DenseNet169	12,643,172	1216	79.54	95.19
DenseNet201	18,277,220	1021	79.89	95.48
DenseNet161	26,681,188	763	79.60	95.10
ShuffleNetV1	949,258	1509	71.42	91.04
ShuffleNetV2	1,355,528	3249	72.80	91.45
MobileNetV2	812,836	3414	64.78	88.47

Table S.5.9: The teacher assistants for TAKD in the CIFAR-100 experiment in Section 5.1. The teacher assistants' performance is often in the middle of the corresponding teacher-student combination.

Teacher	Assistant	Student	Teacher	Assistant	Student	Teacher	Assistant	Student
ResNet110	WRN40 \times 1	ResNet20	WRN40 \times 2	VGG8	MobileNetV2	DenseNet121	ResNet56	MobileNetV2
ResNet32x4	ResNet110	ResNet20	WRN40 \times 2	ResNet8x4	VGG8	DenseNet121	VGG13	ResNet20
VGG13	VGG11	VGG8	ResNet32x4	VGG11	MobileNetV2	DenseNet121	VGG13	VGG8
VGG19	VGG11	VGG8	ResNet32x4	VGG13	VGG8	DenseNet121	WRN40 \times 2	ResNet8x4
WRN40 \times 2	WRN16 \times 2	WRN40 \times 1	ResNet32x4	WRN40 \times 2	ShuffleNetV1	DenseNet121	WRN40 \times 2	ShuffleNetV1
ResNet32x4	ResNet110	ResNet8x4	ResNet32x4	WRN40 \times 2	ShuffleNetV2	DenseNet121	WRN40 \times 2	ShuffleNetV2
			ResNet50	ResNet56	MobileNetV2			
			ResNet50	VGG13	VGG8			
			ResNet50	WRN40 \times 2	ShuffleNetV1			

Table S.5.10: The seed setups in different folders of our GitHub repository for the CIFAR-100 experiment. `./BigGAN` and `./make_fake_datasets` train the BigGAN model and implement the subsampling and filtering modules. `./RepDistiller` implements all other KD methods except TAKD, SSKD, ReviewKD, SemCKD, and SimKD.

Folder	Run 1	Run 2	Run 3	Run 4
<code>./BigGAN</code>	0	1	2	3
<code>./make_fake_datasets</code>	2021	2022	2023	2024
<code>./RepDistiller</code>	2021	2022	2023	2024
<code>./TAKD</code>	2021	2022	2023	2024
<code>./SSKD</code>	2021	2022	2023	2024
<code>./ReviewKD</code>	2021	2022	2023	2024
<code>./SemCKD</code>	2021	2022	2023	2024
<code>./SimKD</code>	2021	2022	2023	2024

To implement SSKD, we follow the default setups in Xu et al. (2020) and the corresponding Github repository. We use the setups suggested by CRD (Tian et al., 2019) to implement other KD methods. Due to limited computational resources, we test fewer KD methods and teacher-student pairs in this experiment.

As for the implementation of cGAN-KD-based methods, we train a BigGAN for 96,000 iterations with the BigGAN-deep architecture (Brock et al., 2019) and a batch size 1,024 following Ding et al. (2022). We borrow the checkpoint of this BigGAN from Ding et al. (2022). DiffAugment (Zhao et al., 2020b) is enabled in the GAN training with the strongest transformation combination (Color + Translation + Cutout). Then, we implement cDR-RS to subsample fake images with the setups suggested by Ding et al. (2022). We choose DenseNet161 to filter fake images with $\rho = 0.9$. We generate 1000 processed fake images for each class (100,000 fake samples in total), which are then used to augment the training set.

cGAN-KD alone and cGAN-KD + X (excluding SSKD): We first initialize student models with their NOKD checkpoints. Then, we train students on the augmented dataset for 240 epochs with the SGD optimizer, initial learning rate 0.01 (decays at epoch 150, 180, and 210 with factor 0.1), weight decay 5×10^{-4} , and batch size 256.

cGAN-KD+SSKD: Initialize student models with their SSKD checkpoints. Then, we train students on the augmented dataset for 240 epochs with the SGD optimizer, initial learning rate 0.01 (decays at epoch 150, 180, and 210 with factor 0.1), weight decay 1×10^{-4} , and batch size 256.

The random seeds used in this experiment are shown in Table S.6.12. Please refer to our codes for more detailed experimental setup.

Table S.6.11: Test accuracy, number of parameters, and inference speed of different neural networks on ImageNet-100. The inference speed is measured by processing 10,000 images with batch size 64 on a single RTX 2080TI. Since DenseNet161 has the highest Top-1 test accuracy, it is chosen as the teacher model f_t in cGAN-KD.

Models	# Params	Inference speed (images/second)	Test Accuracy \uparrow (Top-1)	Test Accuracy \uparrow (Top 5)
VGG8	13,455,460	1546	77.36	92.93
VGG11	18,767,716	1690	81.72	94.29
VGG13	18,952,612	1169	83.03	95.18
VGG19	29,577,124	864	83.41	95.32
ResNet20	278,660	2042	65.25	87.47
ResNet56	861,956	1733	73.20	91.72
ResNet110	1,736,900	1428	75.31	92.03
ResNet8x4	1,234,212	2098	73.19	91.38
ResNet32x4	7,434,532	1855	81.97	94.71
ResNet18	11,221,476	1945	80.22	93.65
ResNet34	21,329,636	1826	81.54	94.47
ResNet50	23,706,596	1576	83.33	95.28
WRN16 \times 2	703,652	2057	72.09	91.06
WRN40 \times 1	570,148	1901	69.98	89.81
WRN40 \times 2	2,255,524	1900	77.67	93.37
DenseNet121	7,050,020	1278	83.22	95.14
DenseNet169	12,644,644	1091	82.93	94.86
DenseNet201	18,278,692	960	82.66	95.15
DenseNet161	26,683,396	732	84.37	95.48
ShuffleNetV1	950,338	1426	75.02	92.07
ShuffleNetV2	1,356,608	1751	77.12	92.72
MobileNetV2	812,836	1805	74.55	91.81

Table S.6.12: The seed setups in different folders of our GitHub repository for the ImageNet-100 experiment. `./make_fake_datasets` generates fake images via a pre-trained BigGAN from Ding et al. (2022) and implements the subsampling and filtering modules. `./RepDistiller` implements all other KD methods except SSKD, SemCKD, and SimKD.

	./make_fake_datasets	./RepDistiller	./SSKD	./SemCKD	./SimKD
Seed	2021	2021	0	2021	2021

S.7. More details of experiments on the Steering Angle dataset

In this experiment, all networks are trained for 350 epochs with the SGD optimizer, initial learning rate 0.01 (decays at epoch 150 and 250 with factor 0.1), weight decay 5×10^{-4} , and batch size 128.

To determine teacher and student models, we first train some popular networks from scratch and their test errors are shown in Table S.7.13. ResNet20, MobileNetV2, WRN16×1, ResNet8x4, WRN40×1, ShuffleNetV1, and ResNet56 are chosen as students due to their high test MAEs. VGG19 is chosen as the teacher model f_t in cGAN-KD due to its lowest test MAE. Some of these neural networks’ checkpoints are used in the implementation of existing KD methods.

We use the SAGAN architecture (Zhang et al., 2019), SVDL+ILI, and hinge loss in the CcGAN training. The CcGAN model is trained for 20,000 iterations with batch size 512, $\kappa = 1123.760$, and $\sigma = 0.028$. DiffAugment (Zhao et al., 2020b) is enabled in the GAN training with the strongest transformation combination (Color + Translation + Cutout). The rest setups are consistent with the official implementation of CcGANs (Ding et al., 2021b). We follow most setups in Ding et al. (2022) to implement cDR-RS, but we disable the filtering scheme in cDR-RS. The reason is the label adjustment module in cGAN-KD functions similarly to the filtering scheme, and the filtering scheme in cDR-RS often leads to much longer training time and sampling time. We choose VGG19 to filter fake images with $\rho = 0.7$. We generate 50,000 processed fake images, which are then used to augment the training set.

The random seeds used in this experiment are shown in Table S.7.14. Please refer to our codes for more detailed training and testing setups.

Table S.7.13: Test MAE, number of parameters, and inference speed of different neural networks on Steering Angle. The inference speed is measured by processing 10,000 images with batch size 64 on a single RTX 2080TI.

Models	# Params	Inference speed (images/second)	Test MAE ↓ (degree)
VGG8	5,228,033	2745	2.07
VGG11	10,540,289	2615	1.38
VGG13	10,725,185	2172	1.43
VGG16	16,037,441	2137	1.49
VGG19	21,349,697	2061	1.06
ResNet20	570,609	2541	5.51
ResNet56	1,153,905	2102	2.68
ResNet110	2,028,849	1635	2.87
ResNet8x4	1,604,641	2737	3.97
ResNet32x4	7,804,961	2135	2.69
ResNet18	11,700,929	2615	1.71
ResNet34	21,809,089	2117	1.41
ResNet50	24,814,657	1478	1.61
WRN16×1	473,281	2636	4.83
WRN16×2	1,022,017	2750	4.51
WRN40×1	862,145	2247	3.87
WRN40×2	2,573,889	2317	3.31
DenseNet121	7,737,537	1412	1.37
DenseNet169	13,595,841	1212	1.54
DenseNet201	19,335,361	1046	1.55
DenseNet161	27,858,721	849	1.35
ShuffleNetV1	1,611,487	2172	3.67
ShuffleNetV2	2,044,125	2158	4.86
MobileNetV2	3,144,961	2278	3.06

Table S.7.14: The seed setups in different folders of our GitHub repository for the Steering Angle experiment. `./cGAN-KD` generates fake images from a CcGAN and implements the subsampling and label adjustment modules. `./cGAN-KD` also implements cGAN-KD. `./RepDistiller` implements feature-based KD methods.

	<code>./cGAN-KD</code>	<code>./RepDistiller</code>
Seed	2020	2020

S.8. More details of experiments on the UTKFace dataset

In this experiment, all networks are trained for 350 epochs with the SGD optimizer, initial learning rate 0.01 (decays at epoch 150 and 250 with factor 0.1), weight decay 5×10^{-4} , and batch size 128.

To determine teacher and student models, we first train some popular networks from scratch and their test errors are shown in Table S.8.15. ResNet20, MobileNetV2, WRN16×1, ResNet8x4, WRN40×1, ShuffleNetV1, and ResNet56 are chosen as students due to their high test MAEs. VGG19 is chosen as the teacher model f_t in cGAN-KD due to its lowest test MAE. Some of these neural networks’ checkpoints are used in the implementation of existing KD methods.

We use the SAGAN architecture (Zhang et al., 2019), SVDL+ILI, and hinge loss in the CcGAN training. The CcGAN model is trained for 40,000 iterations with batch size 512, $\kappa = 900$, and $\sigma = 0.043$. DiffAugment (Zhao et al., 2020b) is enabled in the GAN training with the strongest transformation combination (Color + Translation + Cutout). The rest setups are consistent with the official implementation of CcGANs (Ding et al., 2021b). We follow most setups in Ding et al. (2022) to implement cDR-RS, but we disable the filtering scheme in cDR-RS. The reason is the label adjustment module in cGAN-KD functions similarly to the filtering scheme, and the filtering scheme in cDR-RS often leads to much longer training time and sampling time. We choose VGG11 to filter fake images with $\rho = 0.7$. We generate 60,000 processed fake images, which are then used to augment the training set.

The random seeds used in this experiment are shown in Table S.8.16. Please refer to our codes for more detailed training and testing setups.

Table S.8.15: Test MAE, number of parameters, and inference speed of different neural networks on UTKFace. The inference speed is measured by processing 10,000 images with batch size 64 on a single RTX 2080TI.

Models	# Params	Inference speed (images/second)	Test MAE ↓ (year)
VGG8	5,228,033	2745	5.28
VGG11	10,540,289	2615	5.12
VGG13	10,725,185	2172	5.16
VGG16	16,037,441	2137	5.25
VGG19	21,349,697	2061	5.32
ResNet20	570,609	2541	6.87
ResNet56	1,153,905	2102	7.06
ResNet110	2,028,849	1635	6.77
ResNet8x4	1,604,641	2737	6.68
ResNet32x4	7,804,961	2135	6.36
ResNet18	11,700,929	2615	5.62
ResNet34	21,809,089	2117	5.29
ResNet50	24,814,657	1478	5.91
WRN16×1	473,281	2636	7.25
WRN16×2	1,022,017	2750	6.69
WRN40×1	862,145	2247	6.70
WRN40×2	2,573,889	2317	6.86
DenseNet121	7,737,537	1412	5.34
DenseNet169	13,595,841	1212	5.65
DenseNet201	19,335,361	1046	5.61
DenseNet161	27,858,721	849	5.42
ShuffleNetV1	1,611,487	2172	7.03
ShuffleNetV2	2,044,125	2158	6.87
MobileNetV2	3,144,961	2278	7.16

Table S.8.16: The seed setups in different folders of our GitHub repository for the UTKFace experiment. `./cGAN-KD` generates fake images from a CcGAN and implements the subsampling and label adjustment modules. `./cGAN-KD` also implements cGAN-KD. `./RepDistiller` implements feature-based KD methods.

	<code>./cGAN-KD</code>	<code>./RepDistiller</code>
Seed	2020	2020